RESEARCH ARTICLE

Design and Measurement of a Compact Millimeter Wave Highly Flexible MIMO Antenna Loaded With Metamaterial Reflective Surface for Wearable Applications

B. G. PARVEEZ SHARIFF[1], (Graduate Student Member, IEEE),
TANWEER ALI[1], (Senior Member, IEEE), **PALLAVI R. MANE**[1], (Senior Member, IEEE),
MOHAMMED GULAM NABI ALSATH[2], (Senior Member, IEEE), **PRADEEP KUMAR**[3],
SAMEENA PATHAN[4], **AHMED A. KISHK**[5], (Life Fellow, IEEE),
AND TAIMOOR KHAN[6], (Senior Member, IEEE)

[1]Department of Electronics and Communication Engineering, Manipal Institute of Technology, Manipal Academy of Higher Education, Manipal 576104, India
[2]Department of Electronics and Communication Engineering, College of Engineering Guindy, Anna University, Chennai 603110, India
[3]Discipline of Electrical, Electronic and Computer Engineering, Howard College Campus, University of KwaZulu-Natal, Durban 4041, South Africa
[4]Department of Information and Communication Technology, Manipal Institute of Technology, Manipal Academy of Higher Education, Manipal 576104, India
[5]Department of Electrical and Computer Engineering, Concordia University, Montreal, QC H3G 1M8, Canada
[6]Department of Electronics and Communication Engineering, National Institute of Technology Silchar, Silchar, Assam 788010, India

Corresponding author: Tanweer Ali (tanweer.ali@manipal.edu)

ABSTRACT This article presents a flexible four-element MIMO antenna designed on a thin polyimide substrate to operate at 30.50 GHz for wearable applications. The antenna element structure is a combination of circular rings combined with T-shape stubs. The MIMO antenna isolation is enhanced through a novel decoupling structure consisting of a rectangular stub, four open-ended horizontal strip lines, and two vertical strip lines connecting the ground plane. It provides 22.5 dB isolation, even with conformal orientation. A metamaterial (MTM) reflective surface of 9×9 unit cells is designed and placed below the antenna to improve its radiation characteristics, bandwidth, gain, and specific absorption rate (SAR). The metamaterial unit cell provides a double negative property with a wide stop-band range of 26.27–36.49 GHz. With an MTM surface, the measured bandwidth is 25.2–33 GHz with a maximum broadside gain of 8.90 dBi. The resulting SAR is reduced from 1.71 W/kg to 0.86 W/kg by incorporating MTM reflective surface. The MIMO antenna with MTM improves the bandwidth by 56%, gain by 32.5%, and radiation from bidirectional to broadside, compared to the MIMO antenna without MTM. Also, the antenna is measured and validated for diversity parameters such as Envelope correlation coefficient (ECC), Diversity gain (DG), Channel coefficient loss (CCL), Total active reflection coefficient (TARC), and Mean effective gain (MEG). The reduced SAR and improved antenna performance suggest the proposed MIMO antenna with an MTM reflective surface is suitable for on-body wearable applications in IoT devices, smart watches, headwear, and footwear devices.

INDEX TERMS Decoupling structure, flexible substrate, metamaterial, MIMO, millimeter wave, SAR measurement, wearable antenna, on-body measurement.

The associate editor coordinating the review of this manuscript and approving it for publication was Luyu Zhao.

I. INTRODUCTION

With the increased number of wearable users globally, the market valuation stands at 61.30 billion USD as of 2022. Demand is estimated to rise exponentially, with a compound

annual growth rate (CAGR) of 14.6% from 2023 to 2030 [1]. In wearable devices, wristwear dominates the global market, and other products such as eyewear, headwear, and footwear are also slowly trending. The wristwear devices focus on health monitoring for sports or patients by observing the change in body metabolism, which is measured through sensors. Seamless connectivity with a high data rate is essential for these devices to log data continuously with the other connected devices/systems. For this purpose, various wearable antennas are designed and developed to operate at sub-6 GHz [2], [3]. However, bandwidth at sub-6 GHz is restricted to <100 MHz [4]. The International Telecommunication Union (ITU) allocated a millimeter wave (mmWave) spectrum 30-300 GHz range to enhance the channel capacity, in that K-band (18-27 GHz) and Ka-band (26.5-40 GHz) are least prone to atmospheric conditions [5]. For wearable devices, the flexible antenna should satisfy the following criteria against conformal orientation: minimum operational bandwidth of 1 GHz, a specific absorption rate (SAR) < 1.6 W/kg (Federal Communication Commission (FCC) standard)/ < 2 W/kg (European Union (EU) standard), and stable bandwidth and radiation. For flexible antenna design, highly conformal substrates such as polyethylene terephthalate (PET) [6], flexible printed circuit board (FPCB) [7], liquid crystal polymer [8], and polytetrafluoroethylene (PTFE) are used with thickness ranging from 0.2 to 0.1 mm.

In order to cater higher data rate for wearable technology at mmWave, the MIMO antenna is a preferred choice [9]. However, the design of a flexible MIMO antenna has several challenges against conformal orientation, such as: maintaining good isolation, stable bandwidth, and directional radiation. There are various techniques by which good isolation can be obtained, such as decoupling structures [10], [11], artificial magnetic conductors [12], metamaterial structures [13], self-isolating radiators [14], parasitic elements [15], and hybrid structures (combination of above methods) [16]. Any modification to the antennas ground plane to improve the isolation adversely affects the radiation pattern, generating bidirectional or omnidirectional radiation. In such cases, the human body is exposed to electromagnetic radiation from the antenna, resulting in a higher SAR value. Therefore, the directivity and SAR of a MIMO antenna at mmWave can be improved by incorporating a metasurface/ metamaterial reflectors [17], a split ring resonator (SRR) [18], and a metasurface lens [19], [20] (for directivity).

In [21], a two-element MIMO antenna is proposed for wearable applications where the radiator is a slotted circular patch with defected ground plane structure operating from 24-31 GHz. The slots in the radiator induced the effect of circular polarization. However, in the above design, the substrate used is semi-flexible, and the radiation pattern is omnidirectional. In another two-element flexible MIMO antenna [22], an electromagnetic bandgap (EBG) layer is placed below the antenna to improve the directivity and reduce the SAR. Though the EBG has slightly enhanced the gain from 4.5 to 5.7 dBi, the bandwidth remains narrow. In [13], an 8-element modified antipodal Vivaldi antenna incorporated the SRR and mender line to improve the isolation to 22 dB. However, the design has the limitation of a large antenna profile and SAR of 2.25 per 1g at 28/38 GHz. Another design proposed an eight-element MIMO antenna operating from 4.8-30 GHz for breast cancer detection [23]. However, the above design has limitations of complex design and poor isolation.

The above literature shows that quite a few MIMO antenna designs exist for wearable applications. The MIMO antennas in [13], [21], [22], and [23] have a large antenna profile. In [24] and [25], the design has poor impedance matching with high SAR. The structures in [26] and [27] have low gain. The [22] and [28] have low bandwidth, and the [23] have poor isolation.

Therefore, the above limitations are addressed in this paper by developing a novel, compact, flexible MIMO antenna structure. In addition, a novel decoupling structure is proposed in the ground plane, consisting of a rectangular stub, four open-ended strip lines, and two strip lines connecting the ground planes, achieving isolation greater than 22.5 dB.

The MIMO antenna performance is further improved by incorporating a 9×9 flexible metamaterial (MTM) reflective surface. Though an MTM reflective surface increases the antenna profile, it offers plenty of advantages, such as enhanced bandwidth, gain, and radiation pattern. Also, it aids in suppressing the radio frequency (RF) energy exposure to the human body with reduced SAR. The overall MIMO antenna profile with MTM reflective surface is $22 \times 22 \times 3.45$ mm^3. In terms of wavelength at 30.5 GHz, it is $2.25\lambda_0 \times 2.25\lambda_0 \times 0.35\lambda_0$ indicating that the height of the antenna profile is just 15.5% compared to its length and width. Relatively, the overall antenna profile is comparable with the other existing designs.

For flexible antennas, the choice of substrate greatly defines its performance. Because the flexible/wearable antenna undergoes conformal orientation, the chosen substrate should have good electrical and mechanical properties. There are various flexible substrates used in the literature to design antenna, such as felt-textile [2], liquid crystal polymer (LCP) [8], silicone rubber [27], polyester [29], jeans [30], etc. The detailed analysis of flexible substrates is presented in [31]. Out of these, the polyimide substrate has gained attention in the early 90s to design microcircuits for biomedical applications [32]. Later, polyimides are used in the design of flexible antennas due to their high flexibility, robustness, good electrical and mechanical properties, and high-temperature stability [33]. Therefore, based on the literature, the antenna design in this article uses a polyimide substrate for MIMO design and a metamaterial reflective surface.

The 3D representation of a four-element MIMO antenna and metamaterial reflective surface separated by a distance d_{gap} is shown in Fig. 1(a). Fig. 1(b) shows a photograph of the fabricated prototype antenna. The MIMO antenna with
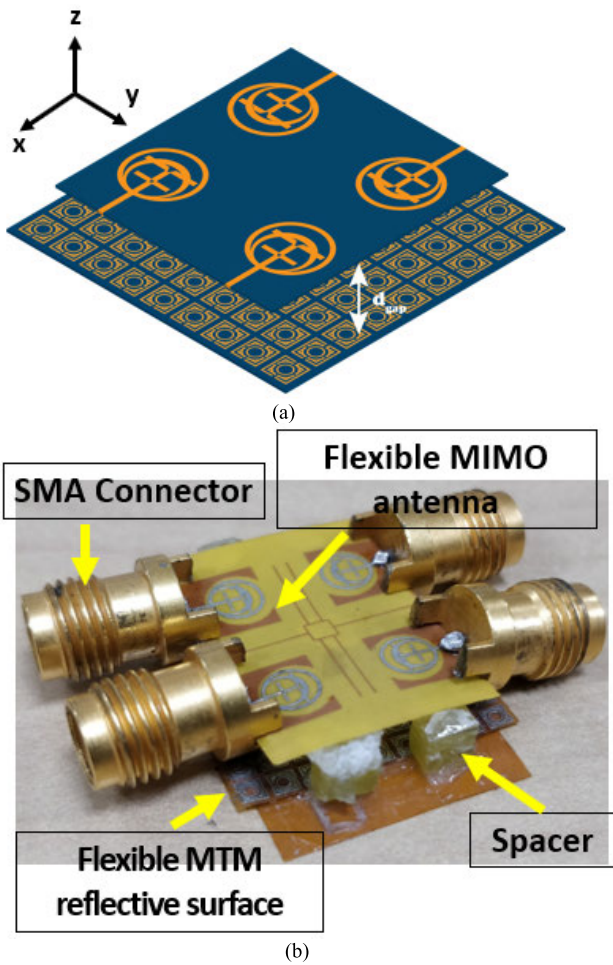
FIGURE 1. (a) 3D sketch of the four-element MIMO antenna above a metamaterial reflective surface and (b) An image of the fabricated antenna with MTM reflective surface below.

FIGURE 2. Evolution stages of the single-element antenna and its S-parameter. (a) Stage 1, (b) Stage 2, (c) Stage 3, (d) Stage 4 (Final), and (e) Reflection coefficient of single-element at respective stages.

an MTM reflective surface achieved 25.2-33 GHz bandwidth, 8.9 dBi gain, directional radiation, and 0.86 W/kg of SAR.

The main contribution of the article is as follows:

1. For a four-element MIMO antenna, the coupling effect is studied through the model current vector diagram, which is minimized by a proposed decoupling structure.
2. A 9 × 9 metamaterial reflective surface is proposed to improve the antenna performance in terms of bandwidth, gain, radiation pattern, and SAR.
3. Performed on-body measurement to verify the real-time variation in the reflection coefficient and further mimicked the phantom model to measure the radiation pattern.

II. DESIGN OF SINGLE-ELEMENT ANTENNA

The design uses a polyimide substrate with a thickness of 0.1 mm, permittivity of 3.5, and a loss tangent of 0.008, which is highly flexible and robust [33]. The antenna is designed to resonate at $f_0 = 30.50$ GHz. The single-element
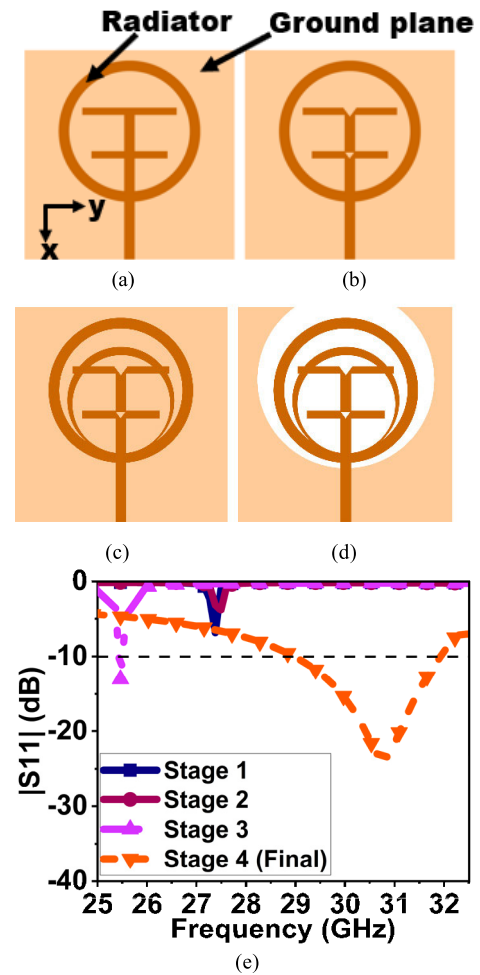
evolved through four stages. Stage 1 combines a concentric ring with two T-shape structures and has a complete ground plane (Fig. 2(a)); Stage 2 introduces slit/slots onto the radiator (Fig. 2(b)); Stage 3 adds an inverted crescent to a radiator (Fig. 2(c)), and in Stage 4 a circular slit is etched in the ground plane (Fig. 2(d)).

The detailed analysis of this single-element antenna is presented in [34] using characteristic mode analysis to better understand the structural and radiation behavior. However, this section briefly explains the theoretical analysis of single-element antenna.

At stage 1 and stage 2 (Figs. 2(a & b)), the impedance matching is poor with low bandwidth, as shown in Fig. 2(e). Adding an inverted crescent in stage 3 (Fig. 2(c)) increases the conductive area, resulting in a downshift of resonance at 25.5 GHz with better impedance matching and reflection coefficient |S11| of 14 dB. To improve the bandwidth and upshift the resonance frequency, a portion of the conductive area is etched from the ground plane in the final stage (stage 4) (Fig. 2(d)) [35], [36]. Therefore, in the final
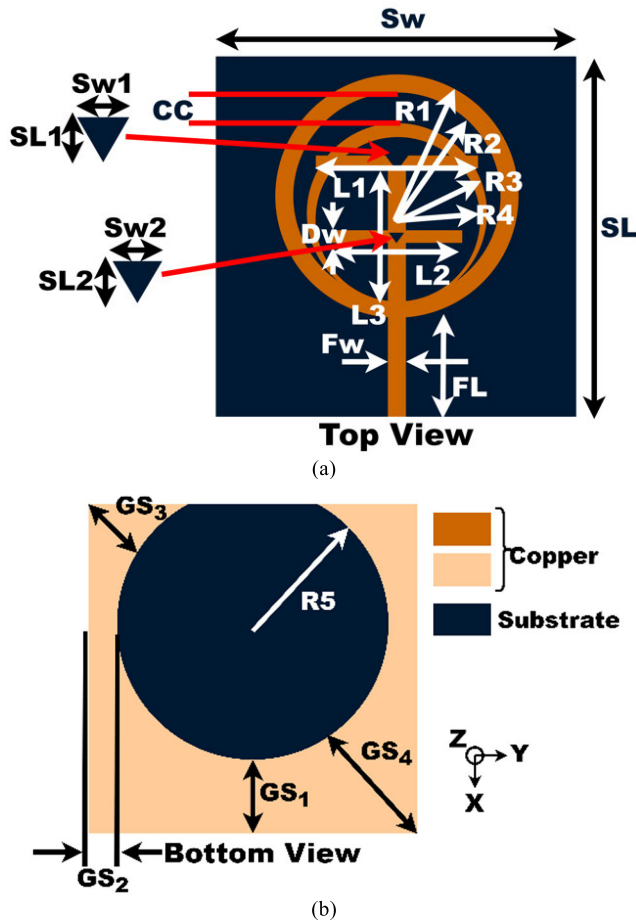
FIGURE 3. Final flexible single-element antenna with dimensions. (a) Top view, (b) bottom view [34].

$$T_{AR} = \left(\pi R1^2 - \pi R2^2\right) + \left(\pi R3^2 - \pi R4^2\right)$$
$$+ (FL \times Fw) + (L1 \times Dw)$$
$$+ (L2 \times Dw) + (L3 \times Dw) \qquad (4)$$

$$T_{AG} = (SL \times Sw) - (\pi R5^2 - A_{SEG}) \qquad (5)$$

$$A_{SEG} = \left(\frac{\theta}{360^0}\right) \times \pi R5^2 - \frac{1}{2} \times R5^2 \sin\theta \qquad (6)$$

The conductive area of the ground plane is etched with a circular slot, where the minor segment of the circle is excluded. Therefore, in calculating the area of the ground plane minor segment of the circle is to be added. From the above-given dimensions in Fig. 3, the θ result in 66°, from which the $A_{SEG} = 0.71$ (Note: all dimensions are in mm) from (6). Further, the total area of the ground plane $T_{AG} = 18.62$ from (5), and the total area of the radiator $T_{AR} = 6.43$ from (4). Adding both the conducting area T_A results in 25.05. Here, k is the tolerance value, which results in 0.42 from equation (2). Substituting all these values to calculate the theoretical value of resonance f_0 in (1) results in 30.06 GHz, which is close to the desired resonance frequency.

III. FOUR-ELEMENT MIMO ANTENNA

The above single-element is extended to a four-element MIMO antenna, as shown in Fig. 4(a). The two elements are adjacent at a distance $TP_1 = 0.62\lambda_0$, and the other two elements are mirrored vertically at a distance $TP_2 = 0.41\lambda_0$. The overall antenna profile is $1.63\lambda_0 \times 1.63\lambda_0$. The initial structure of the ground plane in Fig. 4(b) has a microstrip line NL connected to the ground for all ports. The NL, $CL1$, and $CL2$ form the initial decoupling structure (DCS). This structure provides good isolation between adjacent elements. In this case, the DCS has dual functionality: (i) giving all elements a common ground plane and (ii) behaving as a neutralization structure generating reverse current along the line, reducing the mutual coupling. The neutralization structure can be an arbitrary shape incorporated into the ground or radiator plane [39], [40].

To comprehend the DCS functionality of Fig. 4(b), let us consider the current vector diagram of Fig. 5(a) derived from the surface current vector of Fig. 5(b) when Port-1 (P1) is excited. The general analysis of DCS is as follows: the coupling current J_n^+ indicates the current flowing from (n_{th}) port to ($n_{th} + m$) port, J_m^+ is the reverse current flowing from (m_{th}) port, and J_m^- is the minor coupling current towards (m_{th}) port (which is part of J_n^+), when the port n is excited. In this case, the current J_2^- is the minor coupling current to Port-2 (P2) and J_2^+ is reverse current from Port-2 (P2), generated from J_1^+ on $CL1$ line when P1 is excited. The magnitude of J_2^- and J_2^+ are equal with out-of-phase, resulting in a cancellation, obtaining isolation |S21| of 33 dB throughout the band, as displayed in Fig. 6. The current J_1^+ is confronted with ($J_3^+ + J_4^+$), which is out-of-phase on the NL line, canceling most of the current but generating two coupling currents on $CL2$ as J_3^- and J_4^-. The current density J_4^- is low, so isolation between ports 1 and 4 is moderate at 30 dB. But J_3^- is high, affecting port 3. Therefore,
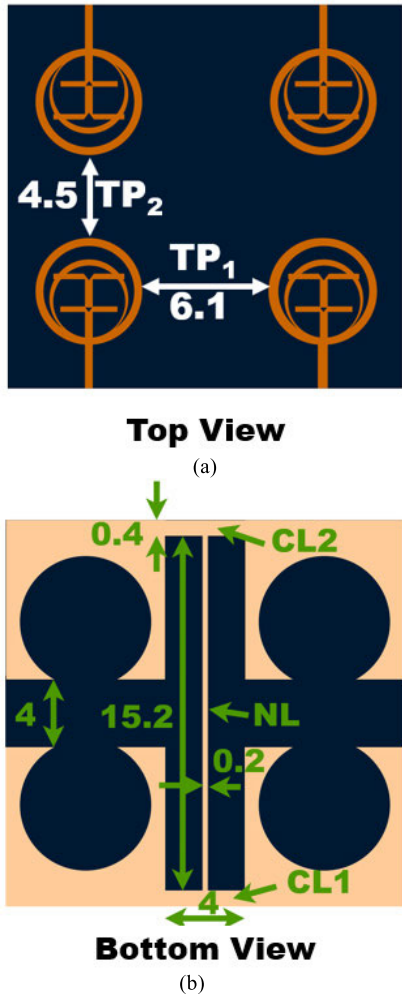
stage, the obtained reflection coefficient at |S11| > 10 dB is 28.80-31.90 GHz, with resonance at 30.70 GHz, as shown in Fig. 2(e). The dimensions of final single-element antenna as follows: R1 = 1.95, R2 = 1.7, R3 = 1.45, R4 = 1.25, R5 = 2.4, L1 = 3, L2 = 2, L3 = 2.09, SL2 = Dw = 0.2, Fw = 0.25, FL = 1.8, CC = 0.62, GS₁ = 1.6, GS₂ = 0.6, GS₃ = 1.24, GS₄ = 2.62, SL1 = SW2 = 0.3, Sw1 = 0.26, and Sw = SL = 6 (all dimensions in mm, R4 circumference is aft by 0.18 mm that of R3 in x-axis), as shown in Figs. 3(a & b).

The design equation to calculate the antenna resonance is a modified equation of [37] and [38]:

$$f_0 = \frac{c}{k \times \frac{2}{\pi} \times T_A \times \sqrt{\varepsilon_r}} \qquad (1)$$

where k is a tolerance value calculated using (2), c is the speed of light in free space (3×10^{11}) in mm, and T_A is the total conducting area, which is the summation of the total area of the radiator (T_{AR}) and ground plane (T_{AG}) (3).

$$k = \sqrt{\frac{14 \times T_A}{\pi \times T_A^2}} \qquad (2)$$

$$T_A = T_{AR} + T_{AG} \qquad (3)$$

FIGURE 4. Proposed four-element MIMO antenna with initial decoupling structure (DCS). (a) Top view, (b) bottom view.
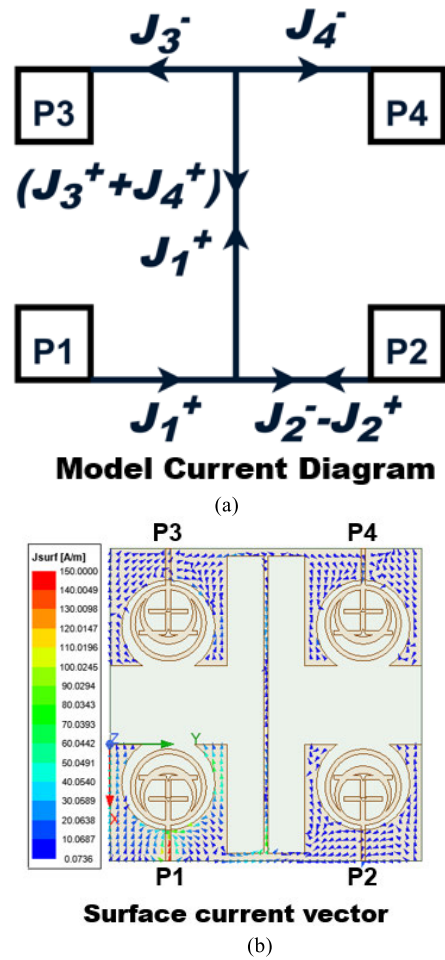

FIGURE 5. Current vector representation of initial DCS structure. (a) Derived model current diagram. (b) Surface current vector.

the isolation |S31| obtained is 20 dB in Fig. 6. A similar analogy can be applied when Ports 2, 3, and 4 are excited individually. The initial DCS has provided good isolation on adjacent and diagonal ports but poor isolation on opposite ports.

Further, to improve the isolation between opposite elements, the DCS structure in the ground plane is modified, as illustrated in Fig. 7. It has a rectangular ring (*NRL*), open-ended strip lines *NL3* to *NL6*, and a ground plane connecting strips *NL1* and *NL2*. The *NL3* and *NL4* traps most of the coupling current between port-1 and port-3. Similarly, *NL5* and *NL6* trap the surface wave current between Ports 2 and 4. The modified DCS provides good isolation between adjacent and opposite elements.

Figs. 8(a & b) is the current model diagram derived from the current vector diagram when P1 is excited for the MIMO antenna with the proposed DCS. In this case, the proposed DCS perturbs the current flow in the structure. As a result, the current J_1^+ in Fig. 8(a) and its coupling current J_2^-, density is higher compared to the reverse current J_2^+ on
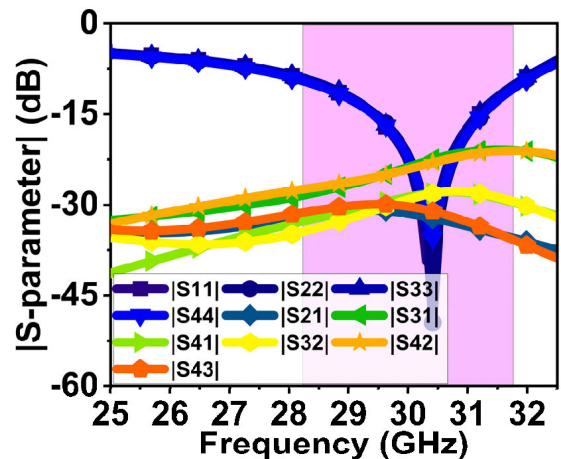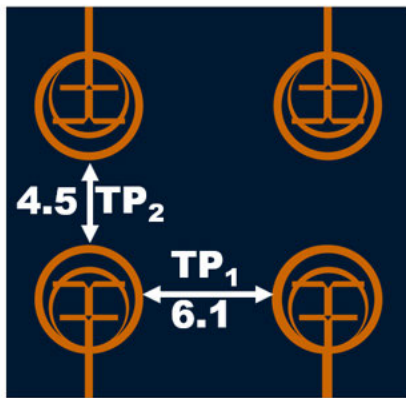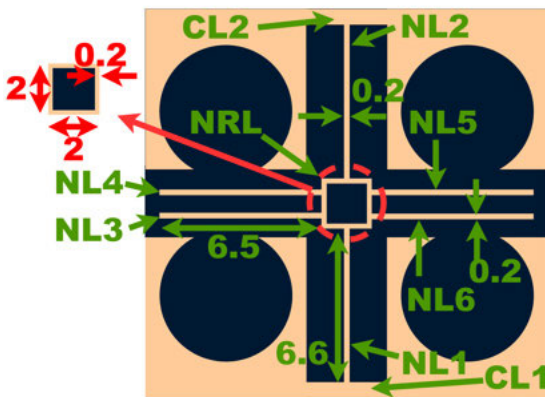

FIGURE 6. |S-parameter| of four-element MIMO antenna for initial DCS.

CL1, so a small coupling can be seen at port 2, resulting in an isolation |S21| of 25 dB, as displayed in Fig. 9. On *NL1, NL2, NL3,* and *NL4* J_1^+ is confronted with reverse current J_2^+, J_3^+, and J_4^+ which regulates the coupling between

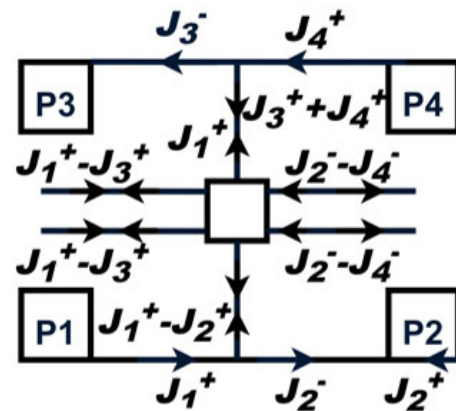**FIGURE 7.** Proposed four-element MIMO antenna with final DCS. (a) Top view, (b) bottom view. *(Note: all dimensions are in mm).*

FIGURE 8. Current vector representation of proposed DCS structure. (a) Derived model current diagram. (b) Surface current vector.

|S31| and |S41|, resulting in isolation of 27 and 34 dB. The proposed DCS structure has slightly drifted the resonance to 30.10 GHz. However, it retained the desired bandwidth of 28.27-31.64 GHz, as shown in Fig. 9.
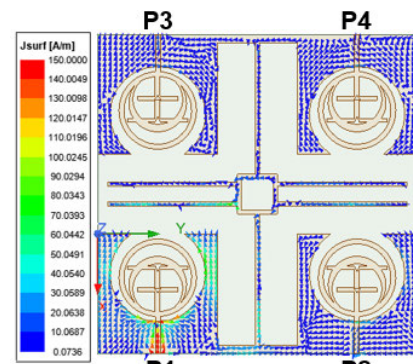
A. EQUIVALENT CIRCUIT OF DECOUPLING STRUCTURE

This section represents the behavior of the proposed DCS structure (i.e., Fig. 7(b)) in terms of distributed lumped LC equivalent circuits. The theoretical approach for equivalent circuits follows the transmission theory with impedance characteristics, as discussed in [41]. For the purpose of analysis, the DGS structure is considered lossless, so the resistance effect is considered negligible. The initial LC values are obtained using the equations presented in [41], which are further tuned to obtain a response close to the simulated results. The circuit is realized using AWR design software. The $CL1$ & $CL2$ in Fig. 7(b) is a microstrip line between Port-1 & 2 and between Port-3 & 4, represented by inductive components ($L1$, $L2$) and ($L10$, $L11$). The NL1 & $NL2$ are rectangular strip lines of DCS represented by inductance $L3$ and $L9$. The narrow gap between these lines and port grounds
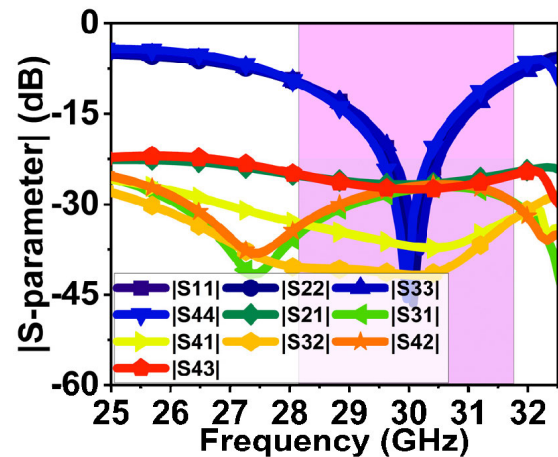

FIGURE 9. |S-parameter| of four-element MIMO antenna for final DCS.

has the capacitance effect, represented as $C1$, $C2$, $C5$, and $C6$ in Fig. 10(a).

The rectangular ring NRL constitutes inductance ($L12$ and $L4$) and the gap by capacitance $C7$. The open-circuited strip line $NL3$ to $NL6$ is represented by inductance $L5$ to $L8$ and the gap by capacitance $C3$ and $C4$. These inductance
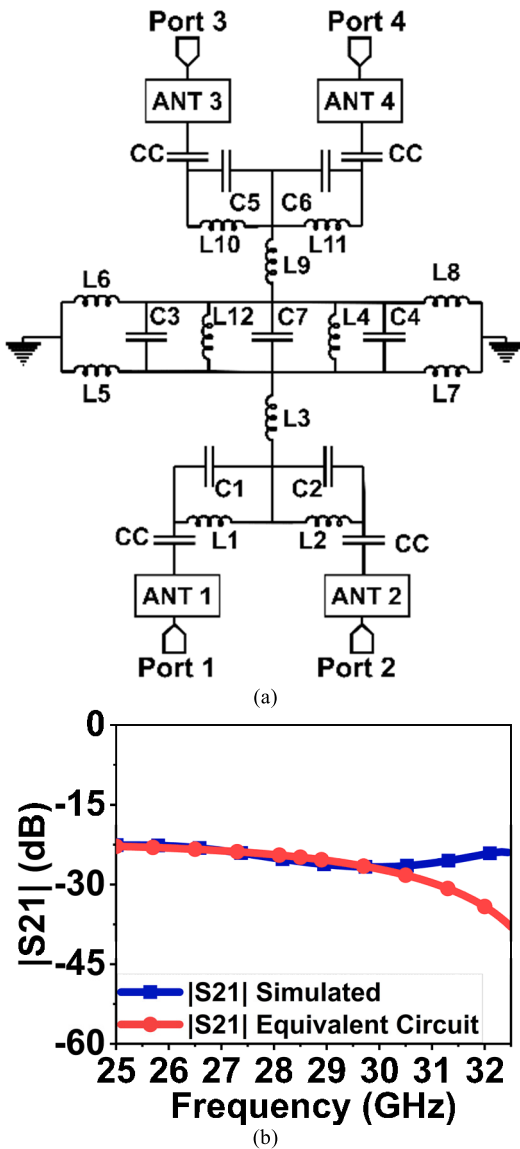
FIGURE 10. (a) Lumped equivalent circuit of proposed decoupling structure (DCS). (b) S-parameter comparison graph of simulated with an equivalent circuit.

FIGURE 11. (a) Bending along the x-axis and its respective |S-parameter| in (c). Bending along the y-axis and its respective |S-parameter| in (d).

and capacitance form the parallel resonance circuit, and the desired response can be obtained by tuning. For this case, the analysis is performed for isolation |S21|. Therefore, the *LC* components primarily contributing to |S21| are *L1, L2, L3, C1,* and *C2,* with values of *0.074 nH, 0.20 nH, 0.018 nH, 0.30 pF, and 0.06 pF.* Whereas all other *LC* values are set to *0.001 nH* and *0.001 pF*. Likewise, to obtain the response for |S31|, *L1, L3, L12, L5, L6, L9, L10, C1, C3, C7* and *C5* need to be tuned. Therefore, the proposed *LC* circuit generates the closest response to the proposed four-port MIMO antenna isolation |S21|, as shown in Fig. 10(b).

B. BENDING ANALYSIS OF THE PROPOSED MIMO ANTENNA

The polyimide substrate is more elastic than other substrates [42], which is why it is used in various RF antenna
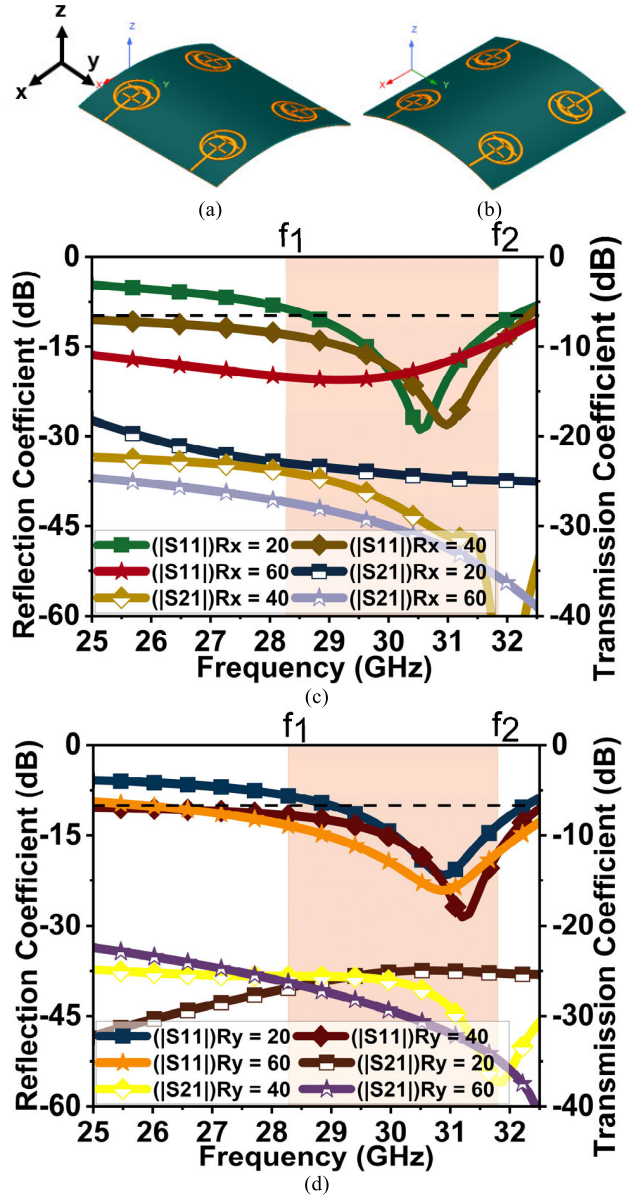
applications [43]. As the proposed four-element MIMO antenna is for wearable applications, the performance of the antenna should not be affected much when it undergoes conformal orientation. Generally, wearable devices are worn on the wrist, forearm, neck, chest, and legs. Out of these, the wrist has the smallest circumference of 155 to 190 mm (for adults). For this reason, the bending analysis is performed along the x- and y-axis (Figs. 11(a &b)) with a radius of 20 to 60 mm in steps of 5 mm.

For the 20 to 50 mm radius along the x-axis, a slight change in resonance can be seen between 30.50 and 31 GHz. For 20 and 25 mm radii, the lower cut-off frequency (f_1) is shifted from 28.30 to 28.72 GHz. The higher cut-off frequency (f_2) is shifted for all the radii to more or less at 32 GHz. The

bandwidth at $|S11| < -10$ is 28.70-31.9 GHz and 28.72-32.1 GHz, respectively, with maximum isolation of 24.9 dB and 26.89 dB. However, for the 30 to 60 mm radius, the bandwidth at reflection coefficient $|S11| < -10$ dB has increased, which is 25-32 GHz, as shown in Fig. 11(c) *(due to brevity in the image, only a few plots are presented in Figs. 11(c & d))*. The isolation for all the radii is well above 20 dB. The result shows that the isolation is improved from 25 to 30 dB for higher radii (40 to 60 mm), which are linearly increasing with frequency.

For the y-axis bend (Fig. 11(b)), the f_2 is increased to 32 GHz for all the radii. Meanwhile, for 20 mm and 25 mm radii, the f_1 is shifted higher, resulting in a reduction in bandwidth of 28.80-32 GHz. For 30 to 60 mm radii, the f_1 is shifted lower, increasing bandwidth from 26.50-32 GHz. The isolation at all the radii is well above 20 dB, as seen in Fig. 11(d). The results reveal that the structure design is versatile enough to give stable results for conformal orientation. The structure reasonably maintains the bandwidth compared to its non-conformal results.

IV. METAMETRIAL REFLECTIVE SURFACE

The metamaterial structures are well known for their equivalent negative permittivity, permeability, and/or refractive index properties. It has been implemented in some antennas as reflective surfaces, metasurface lenses, frequency-selective surfaces, and so on [44], [45]. The proposed four-element MIMO antenna has bidirectional radiation due to defected ground structure. A metamaterial reflective structure is designed to act as a bandstop filter at the resonance f_0 [22], [28]. It is to reduce the back radiation, which in turn regulates the specific absorption rate (SAR).

A. UNIT CELL STRUCTURE

The proposed unit cell has a feature of wide stop-band characteristics with double negative and refractive index properties. It combines rectangular and circular rings on a flexible polyimide substrate of 0.1 mm thickness. The unit cell size is in the range of $\frac{\lambda_0}{10} < d < \frac{\lambda_0}{2}$ simulated by HFSS with primary and secondary boundary conditions. Two Fouquet port excitations are provided on the top and bottom of the boundary. The conductive surface on a substrate is assigned a perfect electric conductor (PEC), which acts as an inductor, and the gap between them gives the capacitance effect. Therefore, the unit cell resonance can be calculated using (7), where L_t and C_t are the total inductance and capacitance of the unit cell.

$$f_0 = \frac{1}{2\pi\sqrt{L_t C_t}} \quad (7)$$

The proposed unit cell with dimensions is shown in Fig. 12(a), and the generalized equivalent circuit in terms of a transmission line (TL) is shown in Fig. 12(b). Here, the substrate (DE) thickness acts as a TL, and the conducting surface of the substrate has L_t and C_t properties, which act as a series of RLC-equivalent circuit between TL. Since there is no conducting surface at the bottom of the substrate, the output
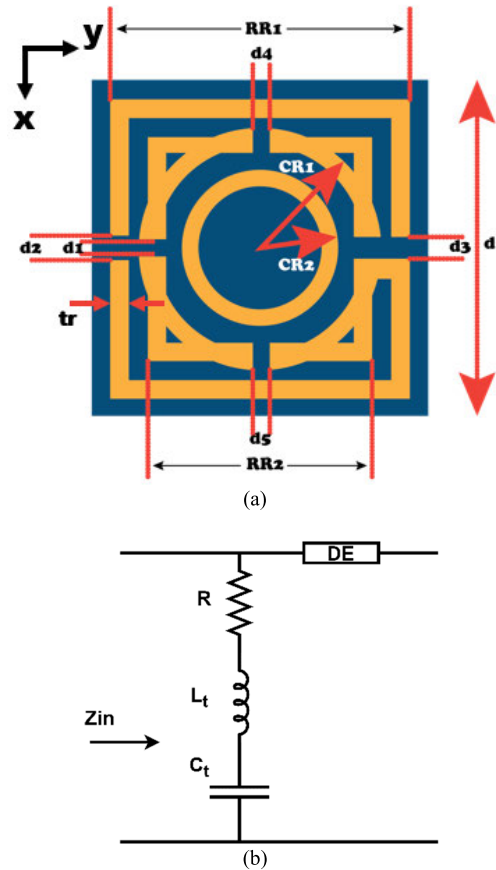

(a)

(b)

FIGURE 12. (a) Proposed unit cell structure with its dimension. RR1 = 1.8 mm, RR2 = 1.4 mm, CR1 = 0.75 mm, CR2 = 0.5 mm, d1 = d4 = d5 =0.05 mm, d2 = d3 = 0.1mm. (b) Generalized representation of unit cell in terms of transmission line.

impedance of the transmission line is open-circuited. The incident wave on the unit cell passes through it until L_t and C_t values are unequal. When these values become equal, the series RLC circuit acts as a short-circuit at the input of the transmission line and reflects the waves. Thus, the unit cell acts as a reflector.

To realize the equivalent permittivity (ε_{eq}), permeability (μ_{eq}), and refractive index (n) of the proposed unit cell, the simulated S-parameter from the HFSS is fed to an analytic or numeric model that uses the same volumetric parameters as the original cell (Thickness and reference plane position from the ports that provide the S-parameters for this model with its ε_{eq} and μ_{eq} varying the model provides similar S-parameters to that from HFSS). This is performed using the MATLAB tool. The unit cell impedance (z) and refractive index (n) are derived from the S-parameter using equations (8)-(10) [46].

$$z = \pm\sqrt{\frac{(1+S_{11})^2 - S_{21}^2}{(1-S_{11})^2 - S_{21}^2}} \quad (8)$$

$$e^{jnk_0 d} = \frac{S_{21}}{1 - S_{11}\frac{z-1}{z+1}} \quad (9)$$

$$n = \frac{1}{k_0 d} \left[\left\{ Im \left[\ln \left(e^{jnk_0 d} \right) \right] + 2m\pi \right\} \right.$$
$$\left. - jRe \left[\ln \left(e^{jnk_0 d} \right) \right] \right] \quad (10)$$

where k_0 is the wavenumber and d is the maximum length of the unit element. The permittivity (ε_{eq}) and permeability (μ_{eq}) derived from refractive index and impedance as:

$$\varepsilon_{eq} = \frac{n}{z} \quad (11)$$

$$\mu_{eq} = nz \quad (12)$$

The unit cell evolved through three stages, as displayed in Figs. 13(a to c). In Stage 1, a rectangular ring $RR2$ of 1.4 mm^2 (thickness $tr = 0.1 \, mm$) is etched inside another ring $RR1$ of 1.8 mm^2 (thickness $tr = 0.1 \, mm$) with a separation of 0.1 mm^2. A circular ring $CR1$ of 0.12 mm thickness (outer radius 0.75 mm and inner radius 0.63 mm) is overlayed on $RR2$. The structure exhibits the stop band behavior at 25.68 GHz for the first stage. The surface current in Fig. 13(d) indicates that the electric field current is concentrated mostly in the outer ring and flows horizontally along the y-axis.

Further, in Stage 2 (Fig. 13(b)) structure is added with another circular ring $CR2$ with 0.1 mm thickness (outer radius 0.5 mm and inner radius 0.4 mm) at the center and slits $d1$, $d2$, and $d3$ at multiple points. Due to these slits, the current started flowing clockwise, mainly in the outer and inner circles (Fig. 13(e)). It resulted in a stopband at 30.35 GHz and a passband at 31.68 GHz. However, the obtained response has narrow stop-band attenuation.

Therefore, in Stage 3 (Fig. 13(c)), two vertical slits, $d4$ and $d5$ are etched, resulting in a wide stop-band from 26.27-36.49 GHz. The surface current in Fig. 13(f) indicates the current concentration in the outer ring. The slit widths of $d1$, $d2$, $d3$, $d4$, and $d5$ are fine-tuned *(0.05, 0.1, 0.1, 0.05, and 0.05 mm)* to obtain the resonance at f_0, as shown in Fig. 13(g). The designed unit cell has the material property of double negative, that is, negative permittivity (ε), permeability (μ), and refractive index in Fig. 13(h).

Due to the complexity of the unit cell, its detailed transmission line representation becomes more complicated. Therefore, an equivalent RLC circuit is designed in Fig. 14(a) to analyze its behavior (R is minimal; hence, it is neglected). However, the initial LC values are calculated using equations defined in [41]. The conducting surface has inductance represented by UL (unit cell inductor), and the gap between them is represented by UC (unit cell capacitors). $UL11$, $UL10$, $UL12$, and $U13$ represent the inductance of the outer ring ($RR1$) and the gap $d2$ and $d3$ by $UC17$ and $UC18$ capacitance. The gap $d1$, $d3$, $d4$, and $d5$ creates four internal structures ($RR2$ and $CR1$), where each of which constitutes an LC tank circuit ($UL2$, $UC7$, $UL3$), ($UL5$, $UC8$, $UL4$), ($UL6$, $UC10$, $UL7$), ($UL9$, $UC12$, $UL8$)) and gap forms capacitance ($UC11$, $UC6$, $UC18$, $UC5$). $UC15$, $UC16$, $UC13$, and $UC14$ form the gap between outer ($RR1$) and internal ($RR2$) ring structures. The center circle $CR2$ is represented by inductor $UL1$, and its capacitance is minimal; hence, it is neglected
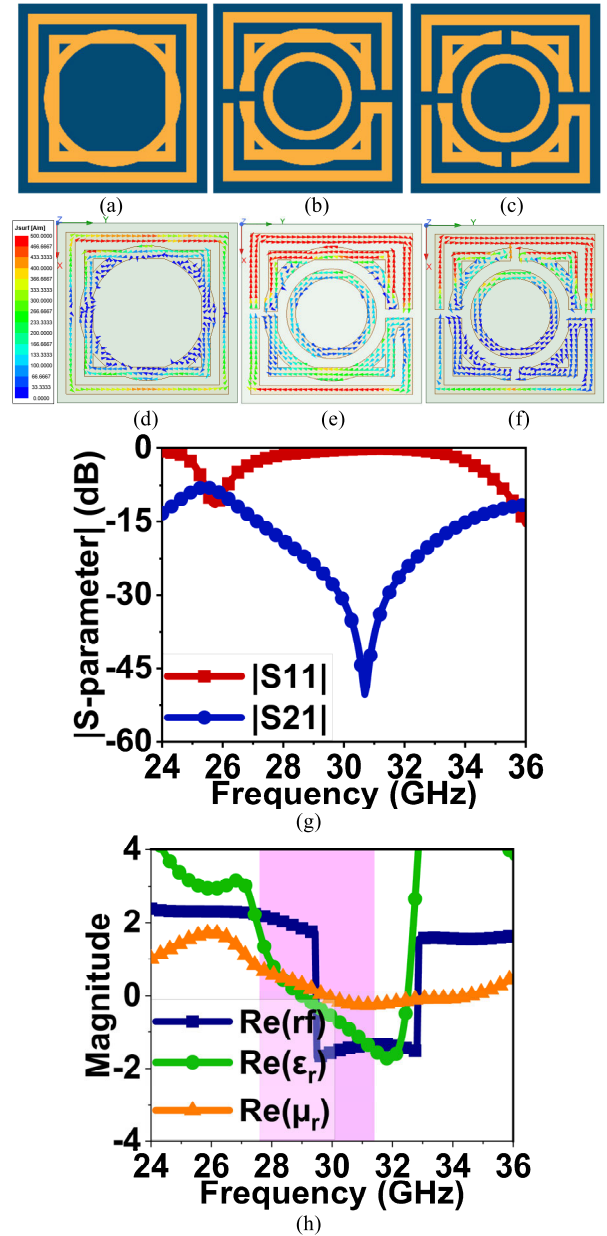

FIGURE 13. Evolution stages of metamaterial unit cell, (a) stage 1, (b) stage 2, (c) stage 3 - proposed unit cell. Surface current vector of a unit cell at various stages, (d) Stage 1 at 25.68 GHz, (e) Stage 2 at 30.35 GHz. (f) Stage 3 at 30.7 GHz. (g) |S-parameter| of proposed metamaterial unit cell. (h) Derived unit cell properties from S-parameters.

in the analysis. Ultimately, the unit cell is arranged in a periodic array structure with a certain gap in the x and y direction. $UC19$, $UC20$, $UC21$, $UC23$, and $UC24$ capacitance depict the gap between adjacent cells. The inductors and capacitors are tuned, and the desired S-parameter is similar to the simulated unit cell, as in Fig. 14(b).

B. PARAMETRIC ANALYSIS OF METAMATERIAL LAYER

The unit cell is expanded to a 2×2 periodic structures along the x-axis and y-axis, separated by distance d_x and d_y, as shown in Fig. 15(a). For $d_x = d_y =$
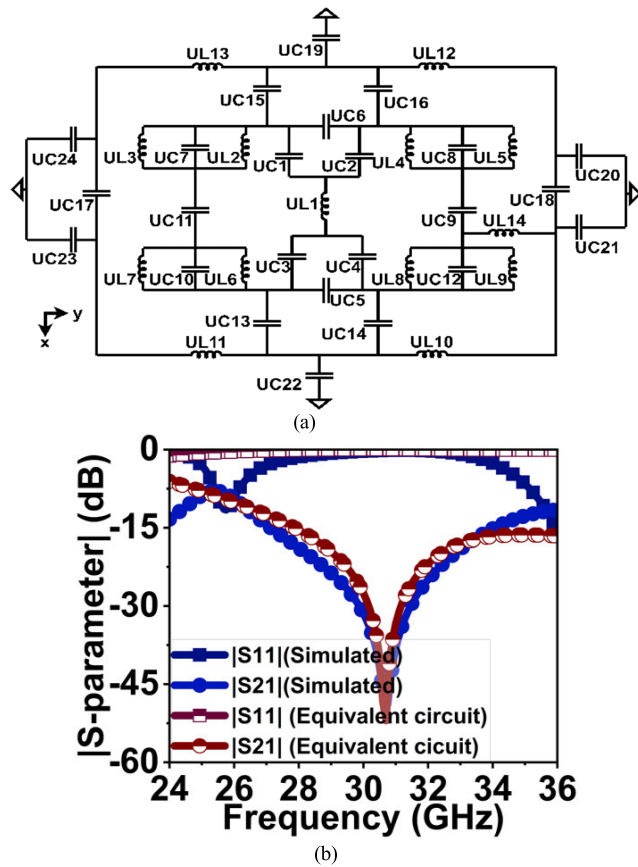
(a)

(b)

FIGURE 14. (a) Equivalent circuit of the unit cell with its inductance and capacitance values are: UC1 = 0.032, UC2 = 0.001, UC3 = 0.001, UC4 = 0.018, UC5 = 1, UC6 = 0.872, UC7 = 0.08, UC8 = 0.095, UC9 = 0.032, UC10 = 0.59, UC11 = 0.001, UC12 = 0.032, UC13 = 0.132, UC14 = 0.18, UC15 = 0.1, UC16 = 0.86, UC17 0.001, UC18 = 0.11, UC19 = 0.2, UC20 = 0.1, UC21 = 0.13, UC22 = 0.11, UC23 = 0.23, UC24 = 0.001, UL1 = 1.45, UL2 = 0.06, UL3 = 0.14, UL4 = 1.24, UL5 = 1.15, UL6 = 0.8, UL7 = 1.49, UL8 = 1.47, UL9 = 0.4, UL10 = 0.23, UL11 = 0.001, UL12 = 0.68, UL13 = 0.49, and UL14 = 0.1 (UC are in pF and UL are in nH (except UL14)). (b) S-parameter comparison of simulated and equivalent circuits of the unit cell.

FIGURE 15. (a) Expanded view of four-unit cells along the x- and y-axis (b) A proposed 9 × 9 periodic MTM structure. (c) |S-parameter| resultant of four-unit cells for varied distances of dx and dy.

0.2 mm, a single transmission zero (TZ) occurred at 30.45 GHz with a wide stop-band from 25.6-36 GHz. For 0.3 mm and 0.4 mm, two TZ are generated at 29.7 GHz and 30.7 GHz/31 GHz in Fig. 15(c) (*due to brevity in the image, only a fewplots are presented*). Similarly, for $d_x = d_y = 0.6/0.7$ mm, two TZ are generated at 29.7 GHz/29.25 GHz and 31.2 GHz/31.4 GHz. From the above parametric analysis, the $d_x = d_y = 0.4$ mm is chosen to prepare the metamaterial reflective surface on $2.25\lambda_0 \times 2.25\lambda_0$ substrate, as depicted in Fig. 15(b). The reason for selecting 0.4 mm is because the two TZ increase the attenuation; also, it has a transmission coefficient of -47 dB at both TZ. Further, the unit cell is expanded to an array of 9 × 9 periodic structures.

The 9 × 9 metamaterial reflective surface is placed below the antenna, separated by a distance of $\frac{\lambda_0}{4} < d_{gap} < \frac{\lambda_0}{2}$ with air as a dielectric medium. The surface current on the unit cell in Fig. 13(f) indicates that the E-field orientation is
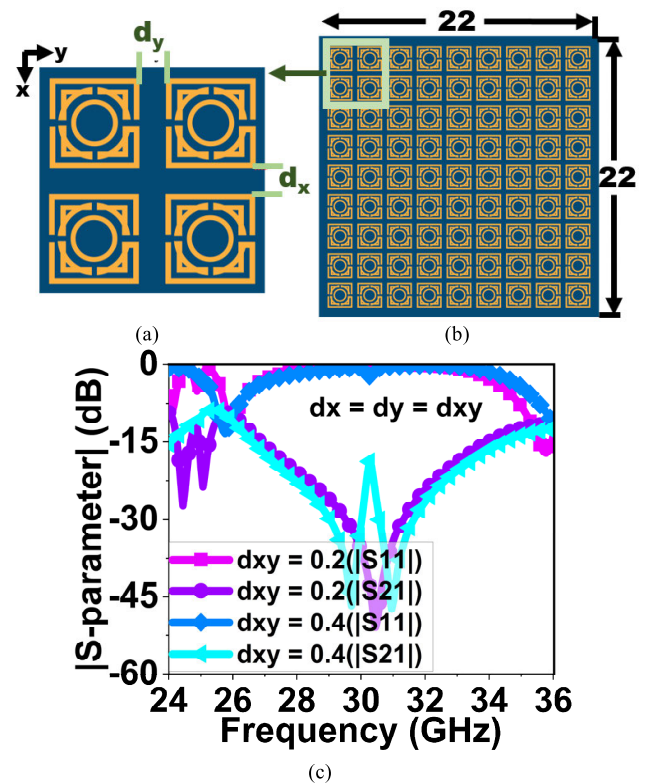
along the y-axis, whereas the antenna E-field is along the x-axis (Fig. 8(b)). For the reflective surface to work correctly with the antenna, the E-field orientation of both structures should be aligned. Therefore, the reflective surface is rotated by 90° in line with the antenna when placed below. Multiple simulation iterations are performed at various d_{gap} distances between 3.44 mm to 3.49 mm to obtain the best results.

C. MIMO ANTENNA PERFORMANCE WITH MTM REFLECTIVE SURFACE

With a d_{gap} of 3.45 mm, the MTM reflective surface has enhanced the antenna performance. The incident and reflected wave are in phase at this distance, leading to constructive radiation in the broadside direction with enhanced gain. It also improved impedance matching over a large spectrum, increasing the bandwidth. The 3D representation of this is shown in Fig. 1(a). The simulated |S-parameter| of the MIMO antenna with an MTM reflective surface without bent is shown in Fig. 16. It has achieved a bandwidth ranging from 23-32.77 GHz with an overall isolation of > 22 dB.

As the antenna is designed for wearable applications, the |S-parameter| performance of the MIMO antenna with an MTM reflective surface is also studied. Fig. 17 shows the conformal along the x-axis and y-axis. The study is performed at three different radii: 40 mm, 50 mm, and 60 mm. When the antenna is bent along the x-axis, a slight drift in the resonance
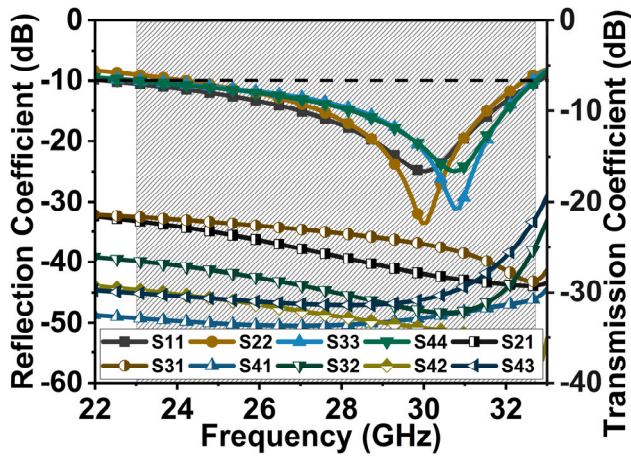
FIGURE 16. Simulated |S-parameter| results of proposed MIMO antenna with MTM reflective surface without bent.
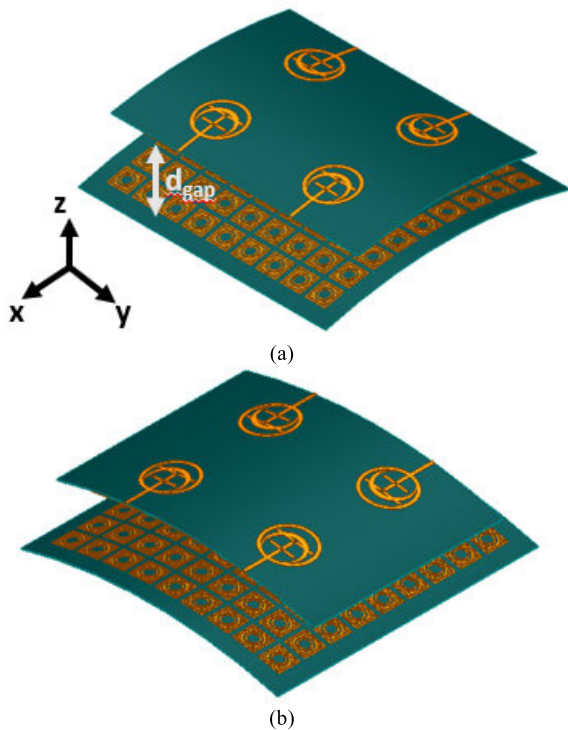

FIGURE 17. Bending analysis of the proposed MIMO antenna with MTM reflective surface. (a) Along the x-axis. (b) Along the y-axis.

FIGURE 18. Simulated |S-parameter| results of the proposed MIMO antenna with MTM reflective surface with bent condition. (a) Along the x-axis. (b) Along the y-axis.

FIGURE 19. Simulated gain of proposed MIMO antenna with MTM under normal and bent conditions with different radii.

is observed at 31.2 GHz. In the bent condition, the incident wave from the MIMO antenna on MTM surface reaches at different incident angles. The change in the incidence angle causes a variable phase in the reflected signal. Summation of this continuous phase-shift reflected wave with the incident wave leads to some distortion. Consequently, the resonance, bandwidth, and gain change are observed in Figs. 17(a), 17(b) and 18.

However, the bandwidth ranges from 26-33 GHz is achieved with an isolation |S21| > 25 dB. In the case of the y-axis bend, the proposed antenna has maintained bandwidth
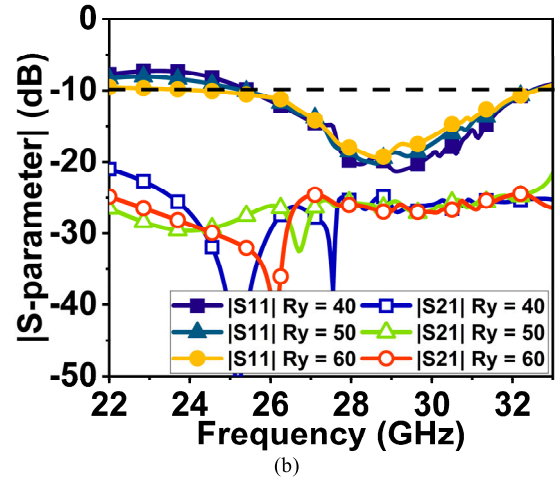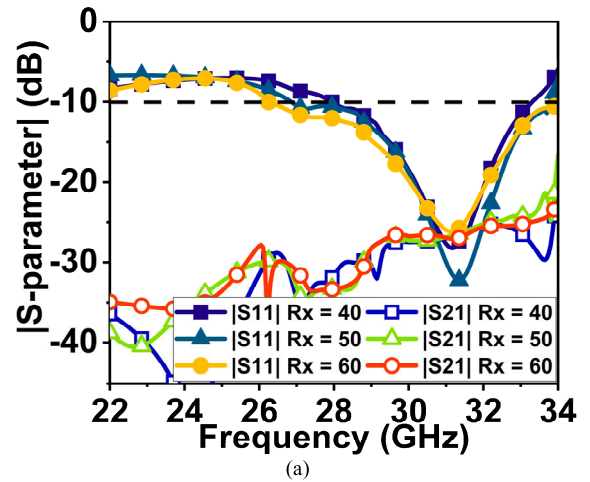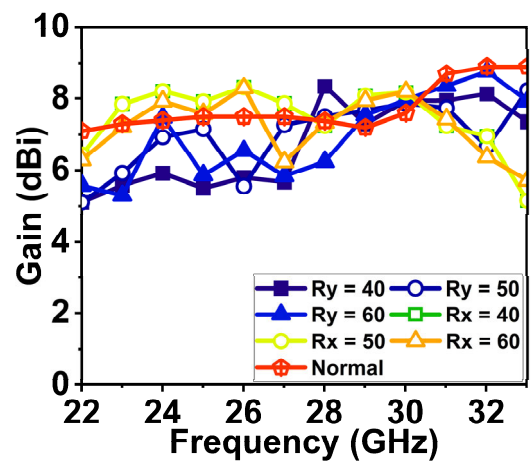
from 24.5-32 GHz with a shift in resonance close to 29 GHz. The isolation |S21| is > 25 dB even in the y-axis bend. Fig. 18 shows the simulated gain of the proposed antenna
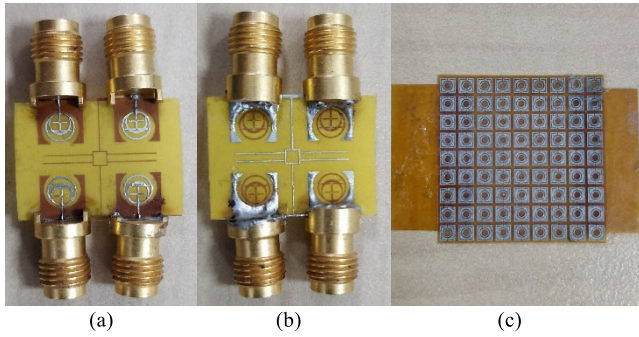
FIGURE 20. Prototype fabricated images. (a) Top view of proposed four-port MIMO antenna, (b) Bottom view of antenna. (c) A 9 × 9 MTM reflective surface.
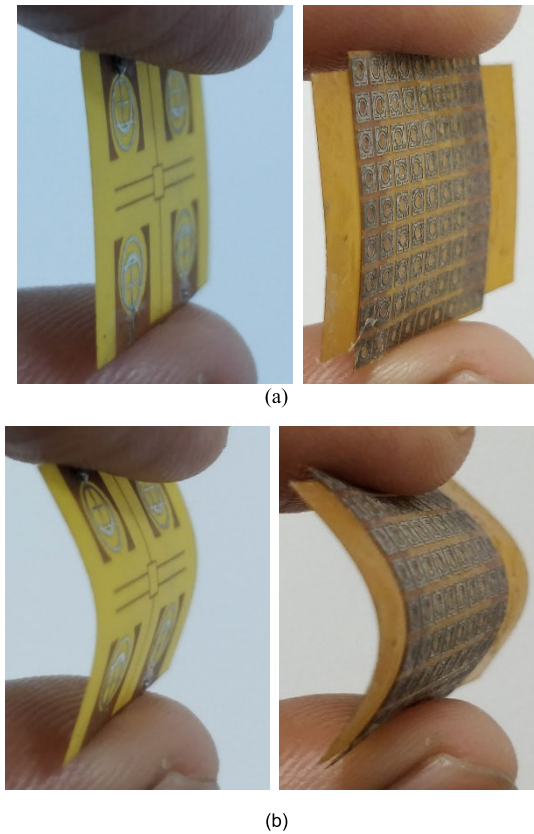

FIGURE 21. Illustration of the conformal orientation of the fabricated antenna. (a) Without conformal orientation. (b) Conformal orientation.

under normal and bent conditions. Under normal conditions, the gain is ranging from 7.2 to 8.7 dBi. However, the gain ranges from 5 to 8 dBi in the bend conditions.

V. RESULTS AND DISCUSSION

The four-element MIMO antenna substrate dimension of Fig. 7 is slightly increased by 3 mm on either side of the y-axis. It provides the area to position spacers, which separates an antenna with an MTM reflective surface. Therefore, the final MIMO antenna dimension is $1.63\lambda_0 \times 2.25\lambda_0$, whereas
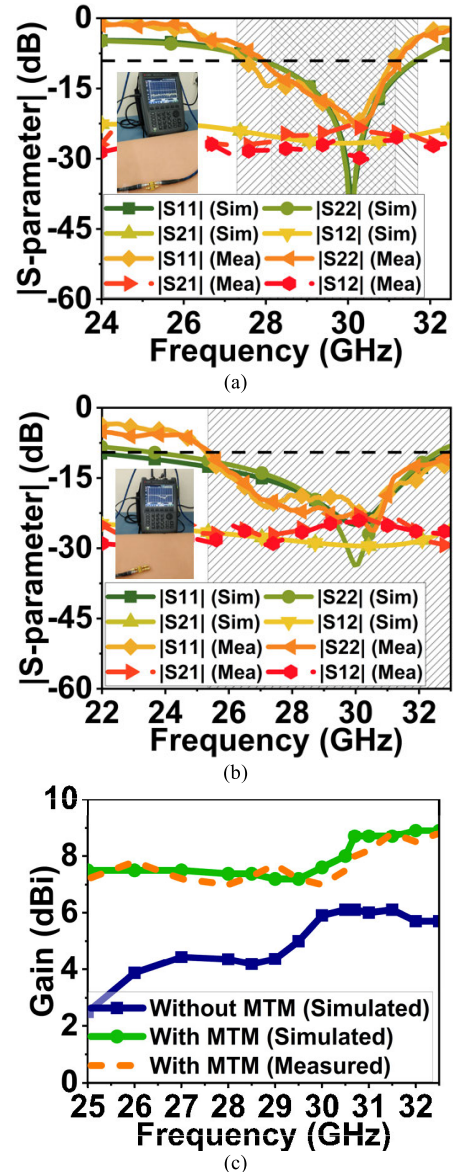

FIGURE 22. Simulated and measured |S-parameter| with gain plot. (a) |S-parameter| without MTM, (b) |S-parameter| with MTM reflective surface. (c) Gain plot.
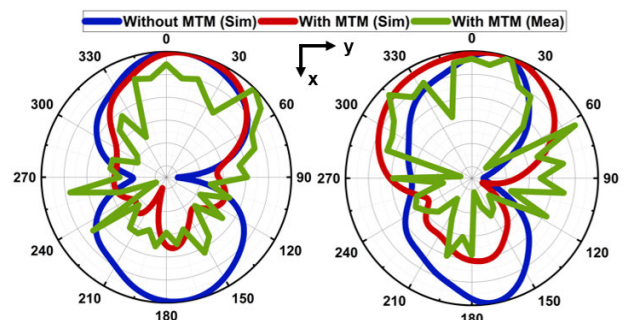

FIGURE 23. Normalized simulated and measured radiation pattern of four-element MIMO with and without MTM structure at f_0. (a) E-plane and (b) H-plane.

the size of the metamaterial reflective surface is $2.25\lambda_0 \times 2.25\lambda_0$.
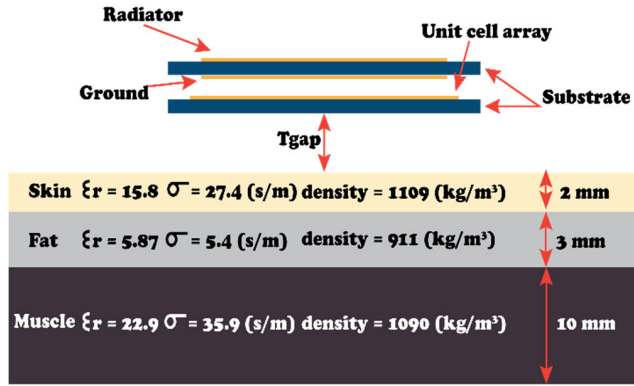
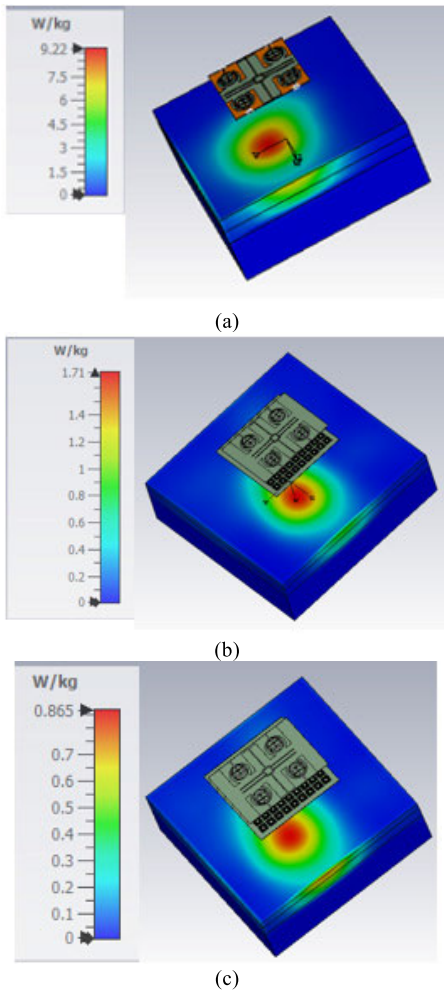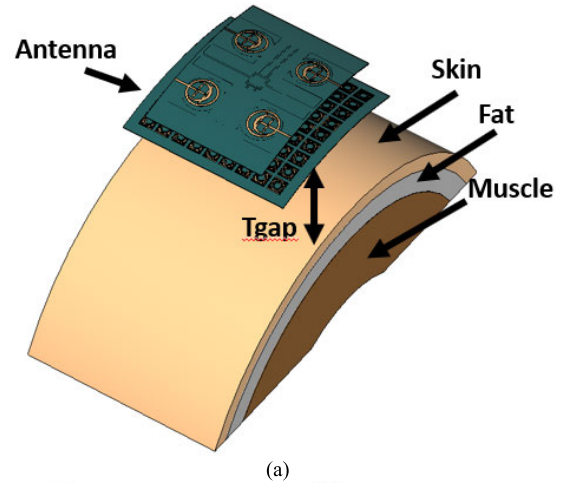**FIGURE 24.** Phantom model of the human wrist for SAR analysis.

FIGURE 25. SAR results at 30.5 GHz: (a) Without MTM at $T_{gap} = 10$ *mm*, (b) with MTM at $T_{gap} = 10$ *mm*, *input power* 100*mW*, and (c) with MTM at $T_{gap} = 10$ *mm*, *input power* 50*mW*.

A. |S-PARAMETER| AND RADIATION PATTERN MEASUREMENT

The proposed four-element MIMO antenna with a 9 × 9 MTM reflective surface is fabricated, as shown in Fig. 20. Fig. 21 illustrates the conformal and non-conformal orienta-
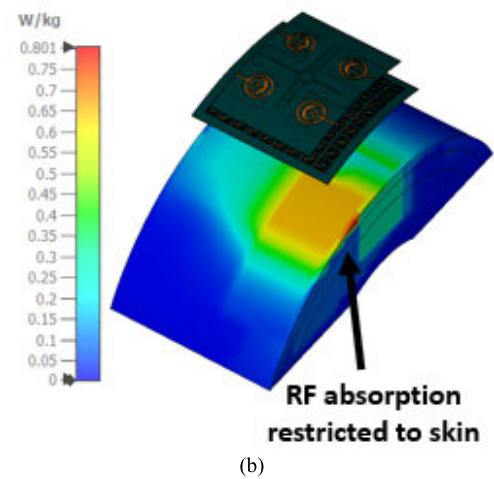

FIGURE 26. Investigation of SAR performance under conformal orientation. (a) Antenna and phantom model representation. (b) Respective SAR results.

tion of the fabricated antenna and MTM reflective surface. The |S-parameter| is measured using VNA N9951A. A 2.4 mm end launch SMA connector (part no. 147-0701-261) from Johnson manufacturer (range 0-50 GHz) is used [47]. The simulation of a four-element MIMO antenna without an MTM reflective surface provided 28.27-31.64 GHz bandwidth with isolation > 25 dB throughout the band, as shown in Fig. 22(a). The measured bandwidth is 27.60-31 GHz with an isolation of > 21 dB.

The four-element MIMO antenna with MTM reflective surface at a distance $d_{gap} = 3.45$ mm resulted in broadside radiation with enhanced bandwidth due to the summation of in-phase waves from the antenna and MTM reflected waves. Therefore, the simulated bandwidth range of the proposed MIMO antenna with MTM is 23-32.77 GHz with an isolation of 25 dB, and the measured bandwidth is 25.20-33.22 GHz with 22.5 dB isolation, as shown in Fig. 22(b). The slight deviation in results is due to fabrication, alignment, and testing tolerance. Also, the exact height of spacers in mm is difficult to achieve, which is why the deviation in measured results can also be seen. However, the variations are well

TABLE 1. Comparative analysis of proposed work with existing designs.

Ref.	Dim	Port	Res (GHz)	BW	Iso (dB)	Gain (dBi)	RP	SAR (W/kg)	ECC	DG	CCL (b/s/Hz)	TARC (dB)	MEG (dB)
[13]	$1.833 \lambda_0$ x $1.65\lambda_0$	8	11	5-40	22	5	Om	1.79	<0.01	-	<0.12	-	-
[21]	$1.9\lambda_0$ x $3\lambda_0$	2	25	23.9-31.4	21	6.1	Om	2.18/1.64	<0.003	>9.9	<0.26	23.4-30.5	0
[22]	$1.52\lambda_0$ x $1.2 \lambda_0$	2	24	23.2-24.8	25	5	Dir	-	<0.2	>9.7	-	-	-
[23]	$0.48\lambda_0$ x $0.48\lambda_0$	8	6	4.8-30	18	6	Om	-	-	-	-	-	-
Proposed MIMO With MTM	$2.25\lambda_0$ x $2.25\lambda_0$	4	30.5	25.2-33	22.5	8.9	Dir	0.86/0.8	<0.3	>9.7	<0.28	22-33	0

Note: Ref − References, Dim − Dimensions, Res − Resonance, BW − Bandwidth, Iso − Isolation, RP − Radiation pattern, Bi − Bidirectional, Om − Omnidirectional, Dir − Directional, *- Not available. *(Note: Diversity metrics are marked for an entire band of interest)*

within the acceptance limit. The maximum gain achieved by the proposed MIMO antenna without MTM is 6 dBi, with an average gain over the band is 5 dBi, as shown in Fig. 22(c). However, the gain of the antenna with the MTM reflective surface is increased to 8.9 dBi (maximum measured). However, the average gain is 7.8 dBi over the entire bandwidth.

The radiation pattern for the prototype antenna is measured in the anechoic chamber, where a millimeter wave horn antenna is used as a reference transmitting antenna. The testing antenna is a prototype fabricated four-element MIMO antenna with and without an MTM reflective surface. The four-element MIMO antenna without MTM reflective surface has bidirectional radiation with half-power beamwidth (HPBW) of 63.56° and 64.86° in E- and H-plane ($\phi = 0°$ and $\phi = 90°$ planes) (Figs. 23(a &b)), respectively. The simulated and measured radiation pattern of the proposed MIMO antenna with an MTM reflective surface has broadside radiation with HPBW of 69.62° and 89.85° in the E- and H-plane, as shown in Figs. 23(a & b), respectively.

B. SPECIFIC ABSORPTION RATE (SAR) ANALYSIS AND MEASUREMENT

The various tissues of the human body have different compositions of water, fat, protein, and salt, which absorb the radio frequency (RF) energy differently. Absorption also depends on the frequency and strength of the electromagnetic energy. However, at mmWave frequencies, the absorption is restricted to the body surface (skin); thus, the penetration will be less [48]. The SAR standards defined by the Federal Communication Commission (FCC) and the International Commission on Non-Ionizing Radiation Protection (ICNIRP) are applicable for frequencies below 10 GHz (i.e., 1.6 W/kg and 2W/kg) [49]. For mmWave frequency, no specific standards are defined. So, the existing standards are being followed to validate the proposed MIMO antenna.

However, the SAR analysis of the proposed antenna is studied and compared with the existing standards. For this, a phantom model of three-layer tissue is created with a length and width of 25×25 mm^2, as shown in Fig. 24. The

thickness of the tissue layer is as follows: skin = 2 mm, fat tissue = 3 mm, and muscle = 10 mm. The skin dielectric can be measured using an open-ended waveguide probe [50]. Its dielectric constant changes over the body at different regions [51]. Therefore, the dielectric constant and electrical conductivity of tissues at f_0 are obtained from the ITIS Foundation database [52]. The permittivity (ε_r) is 15.80, 5.87, and 22.90, and the electrical conductivity σ (s/m) is 27.40, 5.40, and 35.90 for respective tissues.

The antenna structure is kept at varied distances T$_{gap}$ above the phantom model to find the best SAR value. At T$_{gap}$ of 10 mm and input power of 100 mW, the antenna without MTM resulted in a SAR value of 9.22 W/kg per 1g of tissue, as shown in Fig. 25(a) at 30.50 GHz. However, the proposed antenna with an MTM reflective surface at the same T$_{gap}$ and input power resulted in a much reduced SAR of 1.72 W/kg (Fig. 25(b)). Further, the input power is reduced to 50 mW, which results in a reduced SAR of 0.86 W/kg with an MTM structure, as shown in Fig. 25(c). It can also be observed that the radiated energy is spread over the skin tissue and partly in the fat tissue, and there is no penetration to the muscle tissue.

Further, the RF energy absorption by the phantom model under conformal antenna orientation is investigated in Fig. 26(a). For this case, the bent condition of the antenna with MTM surface is taken at the radius of 40 mm, i.e., Ry = 40 mm. The same Tgap is maintained between the antenna and phantom model, as in Fig. 24. Under bent conditions, the proposed antenna with MTM reflective surface has demonstrated approximately similar SAR value as compared to the non-conformal orientation. It resulted in SAR of 0.801 W/kg for the input power of 50 mW. The results in Fig. 26(b) indicate that the RF energy penetration is restricted to the skin layer.

C. ON-BODY MEASUREMENT

As the antenna is proposed for wearable applications, the reflection coefficient variation is studied for on-body measurement. The antenna is slightly bent when placed over the wrist, as shown in Fig. 27(a), resulting in a minor drift
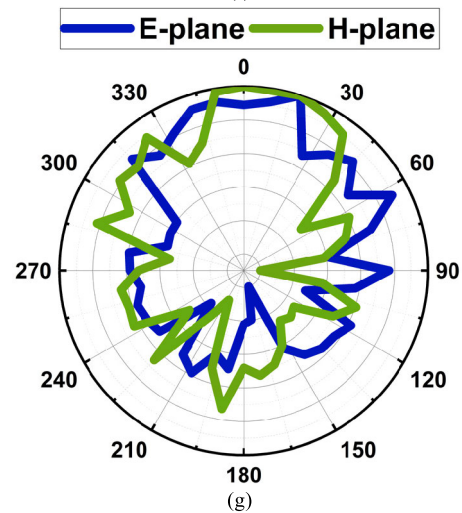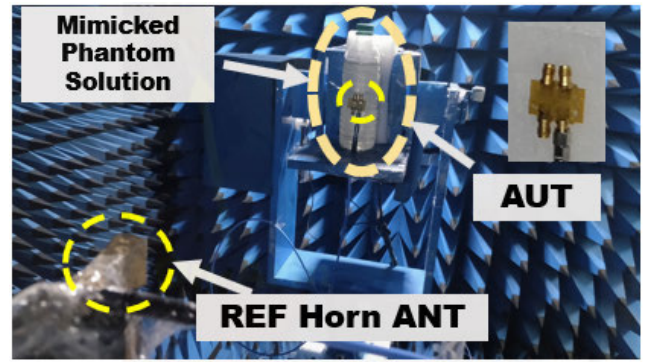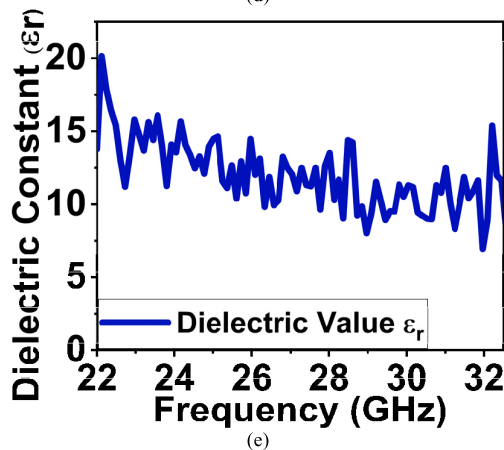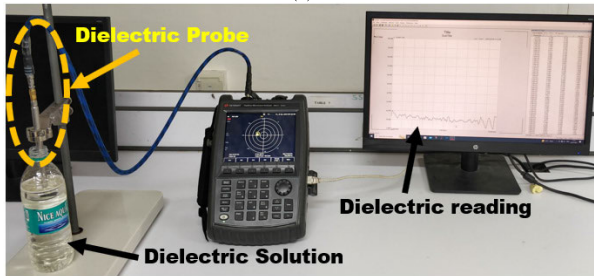
(a)   (b)

(c)

(d)

(e)

FIGURE 27. **(a)** Image of on-body measurement (wrist). **(b)** Image of on-body measurement (arm). **(c)** |S11| results for on-body measurement. **(d)** Dielectric solution measurement setup. **(e)** Plot of dielectric value over frequency of prepared solution. **(f)** Anechoic chamber setup for radiation pattern measurement with a mimicked phantom. **(g)** Measured normalized radiation pattern of on-body measurement.
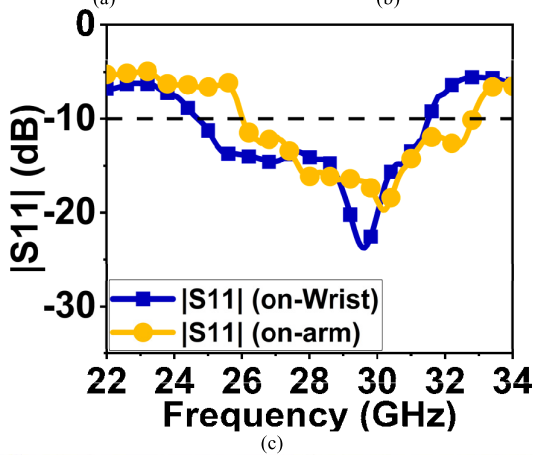

(f)

(g)

FIGURE 27. *(Continued.)* **(a)** Image of on-body measurement (wrist). **(b)** Image of on-body measurement (arm). **(c)** |S11| results for on-body measurement. **(d)** Dielectric solution measurement setup. **(e)** Plot of dielectric value over frequency of prepared solution. **(f)** Anechoic chamber setup for radiation pattern measurement with a mimicked phantom. **(g)** Measured normalized radiation pattern of on-body measurement.

in bandwidth to 24.70-31.54 GHz, as shown in Fig. 27(c). However, the measurement at the arm, as shown in Fig. 27(b), resulted in a bandwidth of 26-32.80 GHz. Therefore, on-body measurement has reduced bandwidth by approximately 1.7 GHz due to the bending effect. The on-body measurement radiation pattern is performed by preparing a solution mimicking the dielectric value of the skin (approx. 15.8). The solution is prepared by a mixture of sucrose in dihydrogen oxide, which is measured using a dielectric probe kit and VNA, as shown in Fig. 27(d). The characteristic of the formulated solution has resulted in an average dielectric value (ε_r) of 12, as depicted in Fig. 27(e). Fig. 27(f) shows the anechoic chamber setup with a bottle filled with solution mimicking the phantom model for radiation pattern measurement. The on-body measurement radiation pattern of the proposed antenna with MTM reflective surface has broadside radiation with HPBW of 62° and 61° in E- and H-plane, as shown in Fig. 27(g).
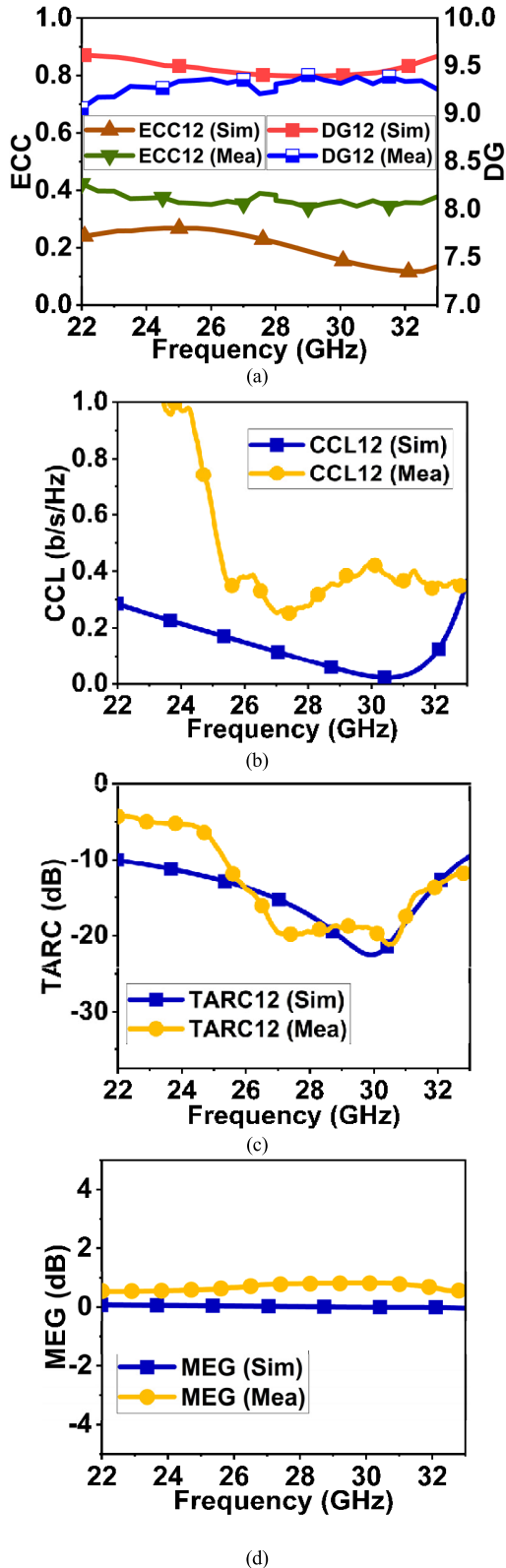
FIGURE 28. Diversity performance of MIMO antenna with MTM structure. (a) ECC and DG, (b) CCL, (c) TARC, and (d) MEG.

D. DIVERSITY PARAMETERS
The diversity parameters are evaluated for a proposed MIMO antenna loaded with MTM reflective surface. The envelope correlation coefficient (ECC) is calculated using the equation defined in [22] from the radiation pattern.

The acceptable value of ECC is < 0.5; for the proposed antenna, ECC resulted in < 0.4, as displayed in Fig. 28(a) *(due to brevity in the figures, only a few plots are shown).* The diversity gain is derived from the ECC; ideally, it should be 10. For the proposed structure, DG > 9.3, as obtained in Fig. 28(a). The channel capacity loss (CCL) of the MIMO antenna should have a bit error rate <0.4 b/s/Hz and be calculated as mentioned in [53]. For the proposed design, CCL < 0.25 b/s/Hz, as shown in Fig. 28(b). The total active reflection coefficient (TARC) is calculated as proposed in [53]. The TARC should be < -10 dB for the band of interest. The proposed antenna is well below the threshold range, as indicated in Fig. 28(c). The mean effective gain (MEG) is calculated using the equation defined in [53]. The proposed structure MEG is zero dB throughout the band of interest, as illustrated in Fig. 28(d).

E. COMPARATIVE ANALYSIS
The performance of the proposed MIMO antenna loaded with an MTM reflective surface is summarized and compared with the existing designs in Table 1. There are very few fully flexible MIMO antenna designs exist to-date. Hence, the comparison is performed with fully flexible and semi-flexible MIMO antennas. The proposed antenna has improved the directivity to broadside direction compared to [13], [21], and [23]. The obtained SAR value is much less than all other designs in Table 1. The proposed antenna has improved the gain compared to all other designs in Table 1. The proposed structure has also improved the bandwidth compared to [22], which also used a reflective surface. The proposed antenna has slightly improved the isolation compared to [13], [21], and [23]. The diversity parameters of the antenna are comparable with [13], [21], [22], and [23].

VI. CONCLUSION
The article has presented a four-element MIMO antenna for wearable applications as it is highly conformal and partially transparent due to the use of a polyimide substrate of 0.1 mm thickness. The single-element structure is a complex combination of circular rings and T-shape structures. Further, the single-element structure has been extended to a four-element MIMO antenna. The isolation of a four-element MIMO antenna has been improved using a decoupling structure in the ground plane, which consists of a rectangular ring, four open-ended strip lines, and two strip lines connecting the ground plane. The overall MIMO antenna profile was $1.63\lambda_0 \times 2.25\lambda_0$. The MIMO antenna has achieved a bandwidth of 27.60-31 GHz. The antenna performance has been improved by using a 9×9 MTM reflective surface with stop-band characteristics from 26.27-36.49 dB with two transmission zeros. The size of the MTM reflective surface was $2.25\lambda_0 \times 2.25\lambda_0$. The four-element MIMO antenna with MTM reflective surface has a wide bandwidth of 25.20-33 GHz with a maximum gain of 8.9 dBi with broadside

radiation. The proposed antenna with an MTM surface has also suppressed the radio frequency energy penetration on the human body, resulting in an SAR of 0.86 and 0.8 W/kg for 1g of tissue for a distance of 10 mm. The results of on-body measurement and diversity parameters have been satisfactory. The proposed antenna is well suited for wristwatches, wristbands, and clothing 5G applications.

REFERENCES

[1] (2030). *Wearable Technology Market Share & Trends Report, 2030.* Accessed: Mar. 11, 2023. [Online]. Available: https://www.grandviewresearch.com/industry-analysis/wearable-technology-market

[2] S. Kumar, D. Nandan, K. Srivastava, S. Kumar, H. Singh, M. Marey, H. Mostafa, and B. K. Kanaujia, "Wideband circularly polarized textile MIMO antenna for wearable applications," *IEEE Access*, vol. 9, pp. 108601–108613, 2021, doi: 10.1109/ACCESS.2021.3101441.

[3] A. Iqbal, A. Smida, A. J. Alazemi, M. I. Waly, N. K. Mallat, and S. Kim, "Wideband circularly polarized MIMO antenna for high data wearable biotelemetric devices," *IEEE Access*, vol. 8, pp. 17935–17944, 2020, doi: 10.1109/ACCESS.2020.2967397.

[4] M. Ikram, K. Sultan, M. F. Lateef, and A. S. M. Alqadami, "A road towards 6G communication—A review of 5G antennas, arrays, and wearable devices," *Electronics*, vol. 11, no. 1, p. 169, Jan. 2022, doi: 10.3390/electronics11010169.

[5] M. Marcus and B. Pattan, "Millimeter wave propagation: Spectrum management implications," *IEEE Microwave Mag.*, vol. 6, no. 2, pp. 54–62, Jun. 2005, doi: 10.1109/MMW.2005.1491267.

[6] H. Qiu, H. Liu, X. Jia, Z.-Y. Jiang, Y.-H. Liu, J. Xu, T. Lu, M. Shao, T.-L. Ren, and K. J. Chen, "Compact, flexible, and transparent antennas based on embedded metallic mesh for wearable devices in 5G wireless network," *IEEE Trans. Antennas Propag.*, vol. 69, no. 4, pp. 1864–1873, Apr. 2021, doi: 10.1109/TAP.2020.3035911.

[7] M. Ur-Rehman, N. A. Malik, X. Yang, Q. H. Abbasi, Z. Zhang, and N. Zhao, "A low profile antenna for millimeter-wave body-centric applications," *IEEE Trans. Antennas Propag.*, vol. 65, no. 12, pp. 6329–6337, Dec. 2017, doi: 10.1109/TAP.2017.2700897.

[8] S. F. Jilani, M. O. Munoz, Q. H. Abbasi, and A. Alomainy, "Millimeter-wave liquid crystal polymer based conformal antenna array for 5G applications," *IEEE Antennas Wireless Propag. Lett.*, vol. 18, pp. 84–88, 2019, doi: 10.1109/LAWP.2018.2881303.

[9] S. A. Busari, K. M. S. Huq, S. Mumtaz, L. Dai, and J. Rodriguez, "Millimeter-wave massive MIMO communication for future wireless systems: A survey," *IEEE Commun. Surveys Tuts.*, vol. 20, no. 2, pp. 836–869, 2nd Quart., 2018, doi: 10.1109/COMST.2017.2787460.

[10] P. Kumar, T. Ali, and M. P. M. M, "Highly isolated ultrawideband multiple input and multiple output antenna for wireless applications," *Eng. Sci.*, vol. 17, pp. 83–90, 2021, doi: 10.30919/es8d570.

[11] M. Hussain, W. A. Awan, E. M. Ali, M. S. Alzaidi, M. Alsharef, D. H. Elkamchouchi, A. Alzahrani, and M. F. A. Sree, "Isolation improvement of parasitic element-loaded dual-band MIMO antenna for mm-wave applications," *Micromachines*, vol. 13, no. 11, p. 1918, Nov. 2022, doi: 10.3390/mi13111918.

[12] A. A. Ibrahim and W. A. E. Ali, "High gain, wideband and low mutual coupling AMC-based millimeter wave MIMO antenna for 5G NR networks," *AEU Int. J. Electron. Commun.*, vol. 142, Dec. 2021, Art. no. 153990, doi: 10.1016/j.aeue.2021.153990.

[13] A. R. H. Alhawari, T. Saeidi, A. H. M. Almawgani, A. T. Hindi, H. Alghamdi, T. Alsuwian, S. A. B. Awwad, and M. A. Imran, "Wearable metamaterial dual-polarized high isolation UWB MIMO Vivaldi antenna for 5G and satellite communications," *Micromachines*, vol. 12, no. 12, p. 1559, Dec. 2021, doi: 10.3390/mi12121559.

[14] F. Wang, Z. Duan, X. Wang, Q. Zhou, and Y. Gong, "High isolation millimeter-wave wideband MIMO antenna for 5G communication," *Int. J. Antennas Propag.*, vol. 2019, pp. 1–12, May 2019, doi: 10.1155/2019/4283010.

[15] K. D. Ayinala and P. K. Sahu, "Isolation enhanced compact dual-band quad-element MIMO antenna with simple parasitic decoupling elements," *AEU Int. J. Electron. Commun.*, vol. 142, Dec. 2021, Art. no. 154013, doi: 10.1016/j.aeue.2021.154013.

[16] M. Irshad Khan, S. Liu, M. Kabir Khan, and S. Ur Rahman, "Eight elements mm-wave MIMO antenna for anti-collision radar sensing application with novel hybrid techniques," *AE Int. J. Electron. Commun.*, vol. 167, Jul. 2023, Art. no. 154687, doi: 10.1016/j.aeue.2023.154687.

[17] D. A. Sehrai, M. Asif, W. A. Shah, J. Khan, I. Ullah, M. Ibrar, S. Jan, M. Alibakhshikenari, F. Falcone, and E. Limiti, "Metasurface-based wideband MIMO antenna for 5G millimeter-wave systems," *IEEE Access*, vol. 9, pp. 125348–125357, 2021, doi: 10.1109/ACCESS.2021.3110905.

[18] K. C. Ravi and J. Kumar, "Multi-directional wideband unit-element MIMO antenna for FR-2 band 5G array applications," *Iranian J. Sci. Technol. Trans. Electr. Eng.*, vol. 46, no. 2, pp. 311–317, Jun. 2022, doi: 10.1007/s40998-022-00486-5.

[19] Z. Wani, M. P. Abegaonkar, and S. K. Koul, "Thin planar metasurface lens for millimeter-wave MIMO applications," *IEEE Trans. Antennas Propag.*, vol. 70, no. 1, pp. 692–696, Jan. 2022, doi: 10.1109/TAP.2021.3098571.

[20] S. Tariq, S. I. Naqvi, N. Hussain, and Y. Amin, "A metasurface-based MIMO antenna for 5G millimeter-wave applications," *IEEE Access*, vol. 9, pp. 51805–51817, 2021, doi: 10.1109/ACCESS.2021.3069185.

[21] R. N. Tiwari, V. Kaim, P. Singh, T. Khan, and B. K. Kanaujia, "Semi-flexible diversified circularly polarized millimeter-wave MIMO antenna for wearable biotechnologies," *IEEE Trans. Antennas Propag.*, vol. 71, no. 5, pp. 3968–3982, May 2023, doi: 10.1109/TAP.2023.3255507.

[22] A. Iqbal, A. Basir, A. Smida, N. K. Mallat, I. Elfergani, J. Rodriguez, and S. Kim, "Electromagnetic bandgap backed millimeter-wave MIMO antenna for wearable applications," *IEEE Access*, vol. 7, pp. 111135–111144, 2019, doi: 10.1109/ACCESS.2019.2933913.

[23] S. N. Mahmood, A. J. Ishak, A. Jalal, T. Saeidi, S. Shafie, A. C. Soh, M. A. Imran, and Q. H. Abbasi, "A bra monitoring system using a miniaturized wearable ultra-wideband MIMO antenna for breast cancer imaging," *Electronics*, vol. 10, no. 21, p. 2563, Oct. 2021, doi: 10.3390/electronics10212563.

[24] M. Ur-Rehman, M. Adekanye, and H. T. Chattha, "Tri-band millimetre-wave antenna for body-centric networks," *Nano Commun. Netw.*, vol. 18, pp. 72–81, Dec. 2018, doi: 10.1016/j.nancom.2018.03.003.

[25] U. Farooq and G. M. Rather, "A miniaturised Ka/V dual band millimeter wave antenna for 5G body centric network applications," *Alexandria Eng. J.*, vol. 61, no. 10, pp. 8089–8096, Oct. 2022, doi: 10.1016/j.aej.2022.01.044.

[26] S. Ahmad, H. Boubakar, S. Naseer, M. E. Alim, Y. A. Sheikh, A. Ghaffar, A. J. A. Al-Gburi, and N. O. Parchin, "Design of a tri-band wearable antenna for millimeter-wave 5G applications," *Sensors*, vol. 22, no. 20, p. 8012, Oct. 2022, doi: 10.3390/s22208012.

[27] T. Govindan, S. K. Palaniswamy, M. Kanagasabai, T. R. Rao, M. G. N. Alsath, S. Kumar, S. Velan, M. Marey, and A. Aggarwal, "On the design and performance analysis of wristband MIMO/diversity antenna for smart wearable communication applications," *Sci. Rep.*, vol. 11, no. 1, p. 21917, Nov. 2021, doi: 10.1038/s41598-021-01326-y.

[28] E. M. Wissem, I. Sfar, L. Osman, and J.-M. Ribero, "A textile EBG-based antenna for future 5G-IoT millimeter-wave applications," *Electronics*, vol. 10, no. 2, p. 154, Jan. 2021, doi: 10.3390/electronics10020154.

[29] M. Wagih, G. S. Hilton, A. S. Weddell, and S. Beeby, "Millimeter-wave power transmission for compact and large-area wearable IoT devices based on a higher order mode wearable antenna," *IEEE Internet Things J.*, vol. 9, no. 7, pp. 5229–5239, Apr. 2022, doi: 10.1109/JIOT.2021.3107594.

[30] A. Kavitha and J. N. Swaminathan, "Design of flexible textile antenna using FR4, jeans cotton and Teflon substrates," *Microsyst. Technol.*, vol. 25, no. 4, pp. 1311–1320, Apr. 2019, doi: 10.1007/s00542-018-4068-y.

[31] G. K. Soni, D. Yadav, and A. Kumar, "Design consideration and recent developments in flexible, transparent and wearable antenna technology: A review," *Trans. Emerg. Telecommun. Technol.*, vol. 35, no. 1, p. e4894, Jan. 2024, doi: 10.1002/ett.4894.

[32] H. S. Haggerty and H. S. Lusted, "Histological reaction to polyimide films in the cochlea," *Acta Oto-Laryngologica*, vol. 107, nos. 1–2, pp. 13–22, Jan. 1989, doi: 10.3109/00016488909127474.

[33] H. R. Khaleel, H. M. Al-Rizzo, D. G. Rucker, and S. Mohan, "A compact polyimide-based UWB antenna for flexible electronics," *IEEE Antennas Wireless Propag. Lett.*, vol. 11, pp. 564–567, 2012, doi: 10.1109/LAWP.2012.2199956.

[34] B. G. P. Shariff, S. Pathan, P. R. Mane, and T. Ali, "Characteristic mode analysis based highly flexible antenna for millimeter wave wireless applications," *J. Infr., Millim., Terahertz Waves*, vol. 45, nos. 1–2, pp. 1–26, Feb. 2024.

[35] M. F. Abedin and M. Ali, "Modifying the ground plane and its effect on planar inverted-F antennas (PIFAs) for mobile phone handsets," *IEEE Antennas Wireless Propag. Lett.*, vol. 2, pp. 226–229, 2003, doi: 10.1109/LAWP.2003.819669.

[36] Z. Ning Chen, T. S. P. See, and X. Qing, "Small printed ultrawideband antenna with reduced ground plane effect," *IEEE Trans. Antennas Propag.*, vol. 55, no. 2, pp. 383–388, Feb. 2007, doi: 10.1109/TAP.2006.889823.

[37] C. A. Balanis, *Antenna Theory: Analysis and Design*, 4th ed. Hoboken, NJ, USA: Wiley, 2016.

[38] A. Toktas, M. B. Bicer, A. Kayabasi, D. Ustun, A. Akdagli, and K. Kurt, "A novel and simple expression to accurately calculate the resonant frequency of annular-ring microstrip antennas," *Int. J. Microwave Wireless Technol.*, vol. 7, no. 6, pp. 727–733, Dec. 2015, doi: 10.1017/s1759078714000890.

[39] Y. Wang and Z. Du, "A wideband printed dual-antenna system with a novel neutralization line for mobile terminals," *IEEE Antennas Wireless Propag. Lett.*, vol. 12, pp. 1428–1431, 2013, doi: 10.1109/LAWP.2013.2287199.

[40] M. Li, L. Jiang, and K. L. Yeung, "A general and systematic method to design neutralization lines for isolation enhancement in MIMO antenna arrays," *IEEE Trans. Veh. Technol.*, vol. 69, no. 6, pp. 6242–6253, Jun. 2020, doi: 10.1109/TVT.2020.2984044.

[41] T. Pei, L. Zhu, J. Wang, and W. Wu, "A low-profile decoupling structure for mutual coupling suppression in MIMO patch antenna," *IEEE Trans. Antennas Propag.*, vol. 69, no. 10, pp. 6145–6153, Oct. 2021, doi: 10.1109/TAP.2021.3098565.

[42] M. U. A. Khan, R. Raad, F. Tubbal, P. I. Theoharis, S. Liu, and J. Foroughi, "Bending analysis of polymer-based flexible antennas for wearable, general IoT applications: A review," *Polymers*, vol. 13, no. 3, p. 357, Jan. 2021, doi: 10.3390/polym13030357.

[43] M. L. S. N. S. Lakshmi, B. T. P. Madhav, H. Khan, and P. V. V. Kishore, "A frequency and pattern reconfigurable asymmetric ground antenna on flexible polyimide material for LTE, Wi-Fi, WLAN and fixed satellite applications," *Flexible Printed Electron.*, vol. 5, no. 2, Jun. 2020, Art. no. 025007, doi: 10.1088/2058-8585/ab8f35.

[44] P. Kumar, T. Ali, and M. M. M. Pai, "Electromagnetic metamaterials: A new paradigm of antenna design," *IEEE Access*, vol. 9, pp. 18722–18751, 2021, doi: 10.1109/ACCESS.2021.3053100.

[45] M. Pallavi, P. Kumar, T. Ali, and S. B. Shenoy, "Modeling of a negative refractive index metamaterial unit-cell and array for aircraft surveillance applications," *IEEE Access*, vol. 10, pp. 99790–99812, 2022, doi: 10.1109/ACCESS.2022.3206358.

[46] A. B. Numan and M. S. Sharawi, "Extraction of material parameters for metamaterials using a full-wave simulator [Education Column]," *IEEE Antennas Propag. Mag.*, vol. 55, no. 5, pp. 202–211, Oct. 2013, doi: 10.1109/MAP.2013.6735515.

[47] *SMA Connector*. Accessed: Feb. 1, 2024. [Online]. Available: https://www.belfuse.com/resources/catalogs/cinchconnectivitysolutions/johnson/ca-ccs-john-mmwave-catalog.pdf

[48] D. K. Ghodgaonkar, O. P. Gandhi, and M. F. Iskander, "Complex permittivity of human skin in vivo in the frequency band 26.5–60 GHz," in *Proc. IEEE Antennas Propag. Soc. Int. Symp.*, UT, USA: IEEE, Jul. 2000, pp. 1100–1103, doi: 10.1109/APS.2000.875414.

[49] G. Ziegelberger, R. Croft, M. Feychting, A. C. Green, A. Hirata, G. D'Inzeo, K. Jokela, S. Loughran, C. Marino, S. Miller, G. Oftedal, T. Okuno, E. van Rongen, M. Röösli, Z. Sienkiewicz, J. E. H. Tattersall, and S. Watanabe, "Guidelines for limiting exposure to electromagnetic fields (100 kHz to 300 GHz)," *Health Phys.*, vol. 118, no. 5, pp. 483–524, 2020, doi: 10.1097/HP.0000000000001210.

[50] Y. Gao, M. T. Ghasr, M. Nacy, and R. Zoughi, "Towards accurate and wideband in vivo measurement of skin dielectric properties," *IEEE Trans. Instrum. Meas.*, vol. 68, no. 2, pp. 512–524, Feb. 2019, doi: 10.1109/TIM.2018.2849519.

[51] S. A. R. Naqvi, M. Manoufali, B. Mohammed, A. T. Mobashsher, D. Foong, and A. M. Abbosh, "In vivo human skin dielectric properties characterization and statistical analysis at frequencies from 1 to 30 GHz," *IEEE Trans. Instrum. Meas.*, vol. 70, pp. 1–10, 2021, doi: 10.1109/TIM.2020.3036767.

[52] (2023). *TISSUE DB? IT'IS Foundation*. Accessed: Apr. 4, 2023. [Online]. Available: https://itis.swiss/virtual-population/tissue-properties/database/

[53] K. Vasu Babu, S. Das, G. Varshney, G. N. J. Sree, and B. T. P. Madhav, "A micro-scaled graphene-based tree-shaped wideband printed MIMO antenna for terahertz applications," *J. Comput. Electron.*, vol. 21, no. 1, pp. 289–303, Feb. 2022, doi: 10.1007/s10825-021-01831-3.

B. G. PARVEEZ SHARIFF (Graduate Student Member, IEEE) received the B.E. degree in telecommunication engineering and the M.Tech. degree in digital electronics and communication systems from Visvesvaraya Technological University, Belagavi, India, in 2007 and 2009, respectively. He is currently pursuing the Ph.D. degree with the Department of Electronics and Communication Engineering, Manipal Institute of Technology, Manipal, India. His research interests include microstrip antenna, array antenna, flexible antenna, and metamaterial structure. He is a member of LMISTE, India.

TANWEER ALI (Senior Member, IEEE) is currently an Associate Professor with the Department of Electronics and Communication Engineering, Manipal Institute of Technology, Manipal Academy of Higher Education, Manipal. He is an active researcher in the field of microstrip antennas, wireless communication, and microwave imaging. He has been listed in the top 2% scientists across the world for the years 2021 and 2022 by the prestigious list published by Stanford University, USA, indexed by Scopus. He has published more than 130 papers in reputed Web of Science (SCI) and Scopus-indexed journals and conferences. He has led seven Indian patents, of which three have been published. He is on the Board of a Reviewer of journals, such as the IEEE Transactions on Antennas and Propagation, IEEE Antennas and Wireless Propagation Letters, and IEEE Access.

PALLAVI R. MANE (Senior Member, IEEE) received the B.E. degree in electronics and communication engineering from the Gogte Institute of Technology, India, in 1996, the M.Tech. degree in digital electronics and advanced communication from the National Institute of Technology, Surathkal, Karnataka, India, in 2002, and the Ph.D. degree in electronics and communication engineering from Manipal Institute of Technology (MIT), Manipal Academy of Higher Education (MAHE), Manipal, in 2014, for the thesis in network coding. She is currently a Professor with the Department of ECE, MIT, MAHE. She has authored several papers at international conferences and journal proceedings. Her research interests include network coding, source, channel coding, communication engineering, and artificial intelligence.
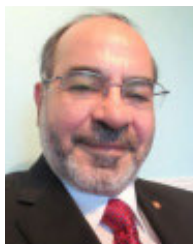
MOHAMMED GULAM NABI ALSATH (Senior Member, IEEE) received the B.E. and M.E. degrees from the College of Engineering Guindy, Anna University, Chennai, and the Ph.D. degree in automotive antennas from Anna University. He is currently an Associate Professor with the Department of Electronics and Communication Engineering, College of Engineering Guindy, Anna University. His research interests include microwave components and circuits, antenna engineering, signal integrity analysis, and solutions to EMI problems.

PRADEEP KUMAR received the bachelor's, M.E., and Ph.D. degrees in electronics and communication engineering, in 2003, 2005, and 2009, respectively. He was a Postdoctoral Researcher with the Autonomous University of Madrid, Spain. He is currently with the University of KwaZulu-Natal, South Africa. He has over 15 years of experience in academics and research. He has held various positions, such as a lecturer, a senior lecturer, an assistant professor, and an associate professor. He is the author of many research papers published in various peer-reviewed journals/conferences. His current research interests include antennas, antenna arrays, and wireless communications. He is registered as a Professional Engineer with the Engineering Council of South Africa. He is serving as a Reviewer/a TPC Member for many journals/conferences, such as IEEE TRANSACTIONS ON ANTENNAS AND PROPAGATION and IEEE ACCESS.

AHMED A. KISHK (Life Fellow, IEEE) has been a Professor with Concordia University, Montreal, QC, Canada, since 2011, and the Tier 1 Canada Research Chair of Advanced Antenna Systems. He has published more than 430 refereed journal articles and 520 international conference papers, and 125 local and regional conference papers. He has coauthored four books and several chapters and was the editor of six books. He offered several short courses at international conferences. His current research interest includes electromagnetic applications. He has recently worked on millimeter-wave antennas for 5G/6G applications, analog beamforming networks, electromagnetic bandgap, phased array antennas, reflectors/transmit arrays, and wearable antennas. In addition, he is a pioneer in dielectric resonator antennas, microstrip antennas, small antennas, microwave sensors, multi-function antennas, microwave circuits, and feeds for parabolic reflectors. He was a member of the AP-S AdCom, from 2013 to 2015, and the 2017 AP-S President. He is a member of several IEEE societies, such as the Antennas and Propagation Society, Microwave Theory and Techniques, Electromagnetic Compatability, Communications, Vehicular Technology Society, and Signal Processing. He is a Senior Member of the International Union of Radio Science Commission B.

SAMEENA PATHAN is currently an Assistant Professor with the Department of Information and Communication Technology, Manipal Institute of Technology, Manipal Academy of Higher Education, Manipal. Her research interests include pattern recognition, medical image analysis, artificial intelligence, and machine learning.

TAIMOOR KHAN (Senior Member, IEEE) received the Diploma (Polytechnic) degree in electronics engineering from the Board of Technical Education, Uttar Pradesh, India, in 2001, the Graduate degree in electronics and communication engineering from the Institution of Engineers, Kolkata, India, in 2005, the master's degree in communication engineering from the Shobhit Institute of Engineering and Technology, Meerut, India, in 2009, and the Ph.D. degree in electronics and communication engineering from the National Institute of Technology Patna, India, in 2014. He is currently an Associate Professor with the Department of Electronics and Communication Engineering, National Institute of Technology Silchar, India. His research interests include printed microwave and millimeter-wave circuits, electromagnetic bandgap structures, dielectric resonator antennas, and artificial intelligence paradigms in electromagnetics.

• • •